
ORIGINAL ARTICLE

This is a non-peer reviewed preprint uploaded to EarthArXiv

Contextual learning improves forest aboveground biomass estimates from UAV-LiDAR: use of tree trait associations.

Jaime C. Revenga¹ | Stefan Oehmcke² | Mana Gharun³
| Flurin Sutter⁴ | Fabian Gieseke² | Katerina Trepekli¹
| Nina Buchmann⁵ | Alexander Damm^{6,7}

¹Institute of Geosciences and Natural Resources Management (IGN), Copenhagen University, Denmark

²Institute of Computer Science (DIKU), Copenhagen University, Denmark

³Institute of Landscape Ecology, Biosphere-Atmosphere Interaction, University of Münster, Germany

⁴Swiss Federal Institute for Forest, Snow and Landscape Research (WSL), Forest Dynamics Research Unit, Switzerland

⁵Department of Environmental Systems Science, ETH Zürich, Switzerland

⁶Department of Geography, University of Zürich, Winterthurerstrasse 190, 8057 Zurich, Switzerland

⁷Eawag, Swiss Federal Institute of Aquatic Science & Technology, Surface Waters – Research and Management, Ueberlandstrasse 133, 8600 Dübendorf, Switzerland

Correspondence

Jaime C. Revenga, Institute of Geosciences and Natural Resources Management (IGN), Copenhagen University, 1350, Copenhagen, Denmark
Email: jar@ign.ku.dk

Funding information

Forest structure analysis and biomass prediction systems are key tools for advancing forest trait-based ecology and ecosystem stewardship. The combination of near-field remote sensing techniques—e.g. Unmanned Aerial Vehicles (UAV) and Light Detection and Ranging (LiDAR) systems—with machine learning (ML) methods enhances the accuracy of tree trait prediction and above ground-biomass (AGB) estimates. In this study, we utilized a UAV-LiDAR system to map the 3D architecture of a Norway spruce forest in Davos, Switzerland, where a field-based inventory served as ground truth data. The objectives of this study were (i) to gain insights into variation and gradients of tree height and (ii) to evaluate whether this knowledge of community structure may prove useful as contextual information to improve predictions of AGB at the individual tree level. To investigate the local association of structural traits, we segmented the point cloud data scene into individual trees and treated tree height as the morphological variable of interest. We then used local indicators of spatial association to determine the extent of significant local context, and defined tree neighborhoods within the forest.

Then, we extracted metrics from the tree neighborhoods and introduced them in a ML regression pipeline to evaluate predictions of individual tree diameter. We set up a regression experiment where the focus is on comparing performance of predictions of tree diameter between the exact same models, either considering neighborhood metrics (i.e. context-aware models), or not. Next, AGB is estimated from tree height derived from UAV-LiDAR, predicted tree diameter and allometry. The benefits of context awareness are assessed in terms of accuracy gained in predicting AGB. For the task of DBH regression, we obtained results of different machine learning methods (i.e. AdaBoost, Lasso and Random Forest) and evaluated these based on nested cross-validation. We applied this approach to two separate tree data sets within the same site, one being clustered and continuous, the other discontinuous and scattered in separate sampling plots. In both cases, we found evidence of enhanced AGB prediction performance in context-aware regressions—RMSE was reduced by 4.0% and by 9.1%, respectively. These findings indicate that gradients in morphological tree traits across the ecosystem proxy for unveiled ecological information that influence tree growth, which can be leveraged to enhance predictions of AGB.

KEYWORDS

aboveground biomass, forest structure, functional trait mapping, machine learning, contextual learning, UAV-LiDAR, quantitative ecology

1 | INTRODUCTION

Aboveground biomass (AGB) is an important component for determining global land carbon (C) budgets. Worldwide, the role of forests is considered essential to understand how atmospheric C circulates between the atmosphere and biosphere [1, 2]. However, current assessments of C-cycling in forest ecosystems present large margins of uncertainty, and contrasting findings exist [3], partly caused by the limited accuracy of AGB estimates [4, 5]. That is why improving quantitative estimates of AGB as well as developing transparent and transferable methods is required [6].

In this context, remote sensing (RS) approaches combined with machine learning (ML) techniques have recently advanced the understanding of the spatial distribution and temporal development of AGB in forests from RS data [7, 8, 9, 10]. Moreover, ongoing endeavors within the RS community aim to reduce the uncertainty of AGB predictions to allow reliable estimates across scales [11]. Continuing such efforts is a necessary step to improve the accuracy of global forest C budgets. Indeed, succeeding in this line of research will improve quantitative estimates of C in forests, and potentially have important consequences in ecosystem science, conservation management [12] and policy making [13]. However, to date, the existence of seemingly equivalent but disparate AGB maps hinders a more frequent use of such data products. This lack of standardization makes it difficult to determine clearly how different AGB maps perform comparatively [6]. To date, AGB maps differ significantly, so it has become particularly relevant to compare data-acquisition techniques [14] and validation procedures [6, 15]. In order to address this shortcoming, broadly accepted validation standards have been proposed in the generation of methods and products of the current decade [6]. However, attaining a community accepted standardization is a considerable undertaking, since the technology, data sources and methods employed between techniques and across scales vary greatly, and new technologies may appear in the future.

In this scenario, Unstaffed Aerial Vehicles (UAV) & Light Detection and Ranging (LiDAR) monitoring systems are regarded as particularly versatile [16], accurate and cost-effective tools [17] to contribute to the task of bridging scales in AGB mapping, particularly covering the scale between *in situ* field-based inventories (i.e. 0-1 ha) and airborne LiDAR datasets (i.e. 0-10⁴ km²) [8, 11]. With an accuracy close to field-based measurements, UAV-LiDAR monitoring provides datasets (i.e. point cloud data, PCD) that allow individual tree phenotyping at an intermediate spatial scale (1-40 ha). The combination of flexibility and accuracy of UAV-LiDAR systems makes possible quantitative phenotyping of single trees across the landscape (e.g. inspection of tree heights across an environmental gradient), providing large and highly accurate datasets to allow accurate analyses [18].

Traditional approaches to AGB research and forest phenotyping from RS data focused on regressions taking only individual tree attributes as predictors (e.g. tree height, tree canopy metrics) [18, 19]. Over time, methods using plot-level metrics (here referred to as "neighborhood metrics") to enhance individual tree trait regression appeared, such as non-linear mixed effects (NLME) methods [20, 21, 22], or competition-based methods [23, 24, 25]. In fact, plot-level information has been reported as beneficial in diverse tree-level regression analyses, e.g. diameter at breast-height (DBH) [22], fuel potential [26] or tree height and crown structural metrics [22, 27, 28].

While both theoretical and technological advances have accelerated the progress of forest AGB research in an unprecedented manner, there is still room for improvement as regards integrating ecological reasoning into AGB research. For instance, scholars argue that understanding local ecological processes requires monitoring biomass of individual trees [24, 29]. However, the opposite idea is seldom discussed: how and to what extent can community ecology processes be harnessed in tree-level AGB regression experiments [23, 25]? We consider this line of work within AGB research as yet relatively unexplored, with some exceptions. Earlier works have proposed to account for the effects of immediate competition pressure on tree growth with either distance-based [25] or distance-independent metrics [30], and judge such approaches beneficial to improve regression results. More recently, Sun et al. (2019) [23]

98 evaluated the potential of distance- and ranking-based tree competition metrics for improving predictions of tree di-
99 ameter growth, and found them outperforming competition-unaware prediction models. Similarly, Zhang et al. (2020)
100 [24] ranked trees by competition levels and applied a quantile regression model to enhance predictions of the tree
101 height-to-diameter ratio.

102 Despite the utility of current methods that leverage neighborhood metrics such as plot-level data (e.g. NLME mod-
103 els) or biotic interactions (e.g. competition-based models), from a RS perspective they remain unsatisfactory in some
104 respects. Many of such methods are not directly transferable to a RS framework because they use understory metrics
105 as predictors [23, 24]. More importantly, questions remain about the optimal scale at which such neighborhood met-
106 rics should be retrieved. We noticed that, in the reviewed studies, the spatial scale at which ecological phenomena
107 operate (e.g. the range at which competition effects are relevant) was not questioned. Instead, the focus is often
108 on plot-level metrics, measured at an arbitrary distance that corresponds to the size of artificially-bounded forest
109 inventory plots [20, 21, 22, 23, 24]. To the best of our knowledge, tree-level AGB and trait assessments considering
110 neighborhood information are currently limited for one or more of the following reasons: (i) they characterize context
111 with uniquely process-specific indices (e.g. competition pressure from immediate neighbors) [23, 24, 25]; (ii) calibrat-
112 ing models with neighbor-metrics retrieved from artificially-bounded inventory plots (e.g. NLME methods) [20, 21, 22];
113 (iii) they do not sufficiently account for the spatial scale at which an ecological phenomenon affect the trait under in-
114 vestigation. Moreover, when the relationship between the plot-level predictors used and any ecological phenomena
115 is described, often ancillary data sources are incorporated (e.g. tree stand age) [24, 31] or non-standardized, poorly
116 quantified forest management terms, e.g. "stand quality", "site index", "dominance index" [21, 24, 31]. These short-
117 comings currently hinder the transferability of such methods to an integrated RS framework, other regions, larger
118 scales or different data collection surveys.

119 A central question in community ecology is how functional trait diversity (e.g. the spatial distribution of tree
120 heights) relates to ecosystem dynamics across environmental gradients [32, 33]. In this regard, current AGB research
121 and mapping initiatives [34, 35] have not yet thoroughly investigated the opportunity to consider spatial patterns [36]
122 of remotely-sensed predictors (e.g. tree height, crown dimensions) to enhance tree-level AGB estimations. These
123 predictors, being subject to a concert of spatially continuous ecological factors—e.g. adaptation to different lighting
124 conditions [37, 38] and soil depth variation [39], or the availability of nutrients and nonstructural carbohydrates [40]—
125 exhibit, as a response, local spatial association (i.e. geographical clusters and gradients of similar tree heights) [41].
126 Such spatial associations of predictors may serve as proxy for the combined effect of the ecological phenomena being
127 considered. Therefore, provided that spatially continuous ecological factors mediate individual tree growth [1, 42]—
128 and the effects of these can be remotely sensed—, it seems plausible to use this information about the local context to
129 improve tree-level AGB assessments. In addition, it appears relevant to examine the spatial extent of the local context,
130 as well as the relationship between context-based traits and individual tree traits.

131 In this framework, ML regression methods seem a sound approach to incorporating a contextual analysis, given
132 that they are flexible, non-parametric methods, commonly integrated into RS forest mapping studies [43]. Such
133 context-based studies [44, 45] have shown in the last decade that the inclusion of information of local context (i.e.
134 information about the surroundings of the target object) may improve model performance. This information can be
135 included in a learning model by either enlarging the receptive field size (i.e. widening the field of view) [46, 47] or by
136 incorporating context-aware features that encode neighboring information into the target object [48] (i.e. a subject
137 tree in our case). In other research fields, such contextual analyses have been successfully incorporated into learning
138 models to improve assessments in, e.g. land-use dynamics [49], Earth system modelling [50] or urban growth [51].

139 To our knowledge, until now there hasn't been a standard RS-based approach to add context into AGB experi-
140 ments. This has hindered the use of context to enhance accuracy of AGB maps. Furthermore, we have not fully inves-

141 tigated how spatial patterns and shifts of tree traits across environmental gradients can show how the environment
142 affects tree structure. Such patterns, as long as can be surveyed and incorporated into a RS framework are relevant
143 to AGB research. Specifically, the question that is still unanswered is how context-awareness can be integrated in a
144 RS framework and leveraged to enhance AGB estimates at the individual tree level.

145 In order to address this question, this study evaluates whether different ML-driven regression models can leverage
146 context-awareness to improve AGB estimates at the individual tree level in a mono-species plantation forest, in a fully
147 integrated RS framework. This requires defining the context without using external ancillary data sources, neighbor-
148 hood metrics from artificially-bounded inventory plots, or metrics from the understory vegetation. The objectives for
149 achieving this aim include: (i) collecting close-range PCD via UAV-LiDAR surveying, (ii) retrieving contextual informa-
150 tion based on the geographic spatial association of tree heights, (iii) developing methods that allowed the context to be
151 defined and incorporated into regression experiments and (iv) evaluating the effect of introducing context-awareness
152 in tree-level AGB estimates.

153 Results showed that AGB prediction performance improves across models as a result of adding context informa-
154 tion. The contribution of this study to current AGB research is the design and evaluation of a method that leverages
155 spatial associations of single tree heights in order to improve AGB estimates from UAV-LiDAR in a fully integrated RS
156 framework.

157 2 | MATERIALS AND METHODS

158 2.1 | Study Area

159 The Seehornwald Davos research site (46° 48' 55.2"N, 9° 51' 21.3" E, 1640 m a.s.l.) is located in a managed subalpine
160 coniferous forest on the western flank of the Seehorn mountain, near Davos, in the Swiss Alps. The site is labeled
161 as a class-1 forest ecosystem station of the Integrated Carbon Ecosystem Station (ICOS) network [52] where regular
162 forest inventory measurements are collected following standardized protocols. The site is covered by spruce trees
163 (*Picea abies* (L.) Karst., > 99.5 %) with an average height and age of 14 m and 100 years, respectively, while some trees
164 reach a height of 40 m and an age of 300 years. The stand parameters at the research site include: tree density: 639
165 \pm 311 tree/ha; basal area: 27.6 \pm 16 m²/ha; mean crown area of dominant canopy: 13.2 m²; mean DBH: 17.7 cm.

166 The site has not been affected by infrastructure development during the 20th century. Since 1930, grazing live-
167 stock in the forest was abandoned, and the site is sustainably managed according to the Swiss Forest Law (1876,
168 revised until 2017) [53]. Maps dating back to 1845 reveal minimal changes within the Davos-Seehornwald forest
169 site, while slight effects of local harvests are noticeable, particularly on steeper slopes of the eastern flank, and forest
170 regrowth at the timberline can also be observed [54]. Patchy vegetation (i.e. dwarf shrubs and mosses) covers around
171 30% of the forest floor (acidic ferrallic podzols), which lies on a mixed silicious and dolomitic bedrock. The research
172 site is part of national (LWF [55], TreeNet [56], SwissFluxNet [57]) and international research networks (ICOS [58],
173 ICP Forests [59], eLTER [60]).

174 The study area considered covers an extension of 33 ha (Figure 1, b), and the terrain conditions are representative
175 of the Alps around the Landwasser valley, i.e. a varying steepness of 23 \pm 14°. The site lies on the eastern flank of
176 the valley, so most of the slopes face west-southwest, i.e. mean slope aspect is 230°.

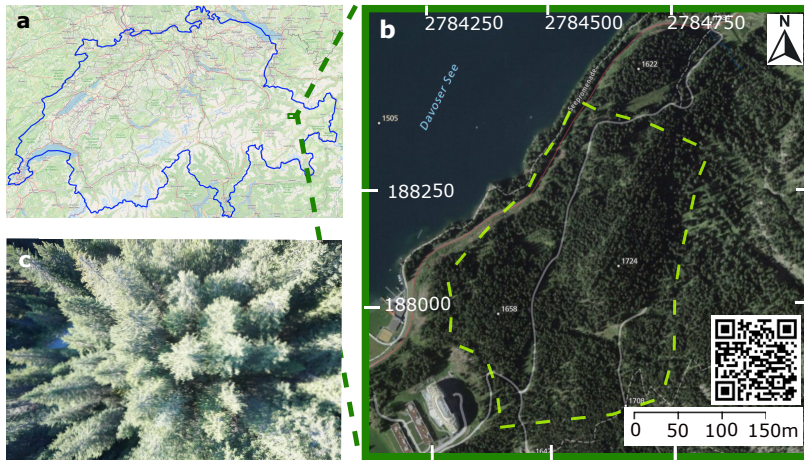


FIGURE 1 a: location of the study site; the blue outline delineates the national territory of Switzerland (adapted from open.sourcemap.com). b: orthoimage of the study site (adapted from swisstopo.admin.ch); coordinate units are in m, with LV95 as a projected reference system; the QR code links to additional information of the study site. The dashed yellow line shows the boundaries of the research site c: RGB image of forest canopy from a nadir angle taken during the survey.

177 2.2 | UAV-LiDAR Survey and Field-Based Measurements

178 We used a UAV-borne LiDAR system mounted to a DJI Matrice 600 Pro payload at a 90° pitch angle, and same heading
 179 and roll as the UAV platform. The system included a discrete infrared LiDAR scanner (M8 sensor, Quanenergy Systems,
 180 Inc. Sunyvale, CA, USA) and the corresponding state-of-the art inertial and navigation systems. In addition, we used
 181 a ground based Global Navigation Satellite System (GNSS, Trimble R8) during the UAV-LiDAR survey, set up in post-
 182 positioning kinematic (PPK) mode, which logged real-time satellite coverage (cf. Revenga et al. 2022 [61] for details on
 183 the airborne and ground system). The coupling of the satellite coverage data with the UAV-based laser and navigation
 184 data produced, allowed the generation of georeferenced point clouds, following Davidson et al. (2019) [62].

185 Data were acquired with a UAV flight height adapted to the terrain and tree height (Figure 2, a), ensuring a >20%
 186 overlap between individual LiDAR scans of ca. 50 m width and 250 points/m² (cf. Revenga et al. 2022 [61] for
 187 additional details on applied flight parameters). The surveys were conducted in October 2021, coinciding with the
 188 end of the growing season. Figure 2 (a) shows the trajectories of the individual UAV-LiDAR flights during the survey
 189 campaign. While the standard survey coverage followed a regular auto-pilot flight grid, certain flight lines had to be
 190 manually piloted to adapt to the topography and local forest structure. The digital elevation model of the study area
 191 is provided in Annex V, to help understand differences in flight heights.

192 The field-based measurements (shown in Figure 2, b) are taken on a yearly basis as part of a long-term ecosystem
 193 monitoring initiative—jointly organized by ICOS [58] and the Swiss Federal Institute for Forest, Snow and Landscape
 194 Research (WSL) [55]. Based on standardized methods (i.e. *Sanasilva Inventory* protocol [63]), expert field workers
 195 monitor tree crown status in terms of color and density, focusing on three groups of indicators: variations in size,
 196 density and color. The number of trees that have died since the previous survey, as well as the new ones that reached
 197 a minimum DBH of 5 cm are also recorded [64]. Tree height and DBH are monitored with a high-precision digital
 198 rangefinder (i.e. Vertex Laser Geo) and a standard calliper, respectively.

199 We treated two different datasets separately as ground-truth measurements within the same study area: control

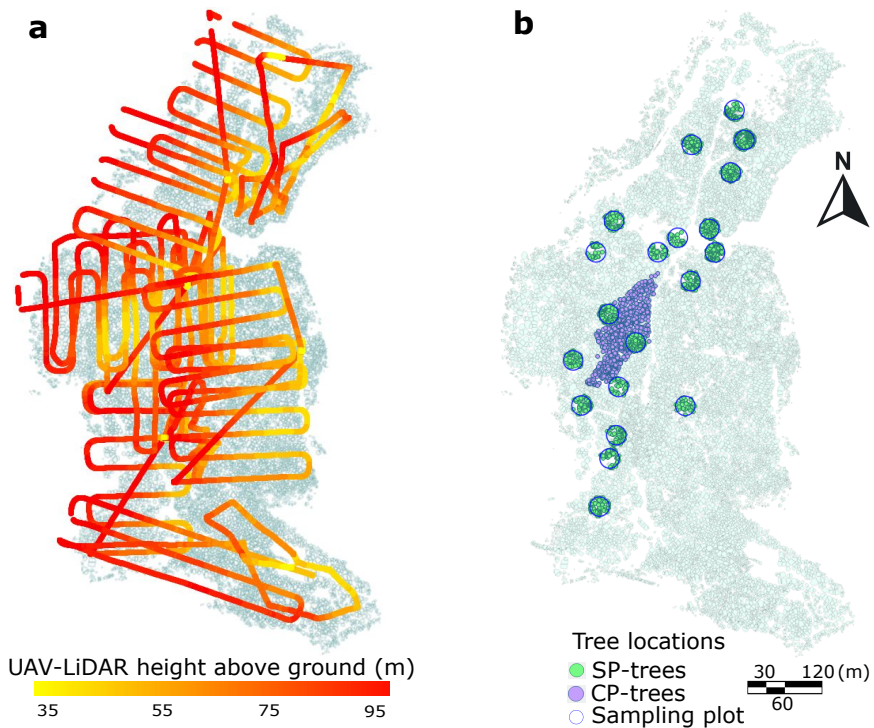


FIGURE 2 a: trajectories of individual flights during survey of the Unstaffed Aerial Vehicle (UAV) Light Detection and Ranging (LiDAR) sensor; color gradient indicates height above ground during survey. b: spatial distribution of field-based forest inventory. Dots represent the locations of the ground-truth labels. The sampling plot-trees (SP-trees, $N = 1635$ trees) are shown in green; the control plot-trees (CP-trees, $N = 845$ trees) are shown in purple. In both a and b, the underlying polygon dataset shows the individual tree canopies (ITC) after the canopy height model (CHM) segmentation.

200 plot trees (CP-trees, 4 adjacent monitoring units) and sampling plot trees (SP-trees, 20 scattered units of 15 m radius).
 201 The only difference between the two datasets is that SP- and CP-trees are monitored by different research groups
 202 on the field. Several factors led us to consider both datasets separately: (i) the CP dataset is clustered and spatially
 203 continuous, while the SP dataset is spatially discontinuous and distributed along the study site (Figure 2, b); (ii) the
 204 two datasets present significant differences in morphological trait distribution (see Supporting Information, Annex IV);
 205 (iii) the variability in context metrics between the two datasets varied markedly; (iv) the field-based instrumentation
 206 and protocols used for monitoring presented minor differences between both datasets. Figure 2 (b) shows the spatial
 207 distribution of the field-based forest inventory. The CP tree position was recorded using a Leica GPS1200 total station.
 208 The location and size of the sampling plots were defined according to ICOS protocols [65]. The center location of the
 209 SP plots was determined using a GNSS Leica CS20 (antenna GS15) with a real-time kinematic (RTK) signal (accuracy
 210 measurements ranges from 0.03m to 0.7m). Next, the trees in the SP plots were positioned by measuring the azimuth
 211 with a field goniometer, while the horizontal distance and the inclination from the plot centers was determined using
 212 a Vertex Laser Geo meter. The accuracy of foot location of trees in the SP plots is within 0.5 m and 1.2 m. The field-
 213 based inventories used as ground-truth contain measurements taken between October 2019 and July 2021. The
 214 changes in structural traits of max. two years between field-based measurements and UAV-LiDAR data acquisition

215 were considered negligible for the purposes of this study (i.e. no disturbance events occurred).

216 2.3 | Data Processing

217 The workflow followed in this study is presented in Figure 3. Initially, the PCD generation followed the approach de-
218 scribed in Revenga et al. (2022) [61]. The resulting PCD scene was normalized and rasterized to obtain a canopy height
219 model (CHM), which in turn was subject to individual tree crown segmentation [66] producing a two-dimensional poly-
220 gon dataset. For the CHM segmentation, we utilized a watershed algorithm that is specifically designed for coniferous
221 forests [66] (implemented in the LiDAR360 software [67]). The match between field-based measurements and indi-
222 vidual tree crown (ITC) polygons was conducted based on the closest distance between the field-based GNSS point
223 measurement and the ITC polygon centroid.

224 In order to ensure that only the LiDAR-detected trees would be accounted for in the regression experiment, a
225 pre-processing manual task was undertaken (marked * in Figure 3). First, understory trees that passed unnoticed
226 to the UAV-LiDAR survey were removed. Second, we filtered clumped trees based on tree height by selecting the
227 field-based measurement of the highest tree when two measurements were less than 1 m apart, while removing the
228 measurement of the other tree. Third, we corrected for a crown shift effect, i.e. some high and skewed trees were
229 affected by the presence of a smaller neighboring tree (affecting about 5% of trees) being closer to its corresponding
230 ITC polygon centroid, thus introducing a wrong match between the field-based measurement and the LiDAR-derived
231 metrics.

232 Afterwards, using the LiDAR-derived height as polygon attribute, we calculated the distance at which the spatial
233 autocorrelation of tree height was most significant in order to define the optimal neighborhood size (as explained
234 in Section 3.1). Once the optimal neighborhood size had been defined, we conducted the local indicators of spatial
235 association (LISA) analysis [36, 41] and outlier analysis [68, 69] to retrieve neighborhood metrics. Finally, two separate
236 supervised regression experiments were performed, in order to predict DBH based on LiDAR-derived metrics: one
237 including the neighborhood metrics (context-aware regression), the other without taking those metrics into account
238 (context-unaware regression). Finally, AGB was estimated from the predicted DBH via an allometric function (as
239 defined in Eq. 5).

240 In parallel, we conducted a second task to characterize the morphometry of tree assemblages (i.e. groups of
241 adjacent trees fulfilling a specific criterion of height similarity, as explained in Section 2.6) stemming from the ITC
242 polygon dataset. Prior to the morphometric analysis of tree assemblages, a second pre-processing task was conducted
243 (marked ** in Figure 3). First, ITC polygons were merged based on either local Moran's I_i [36] or SL_i [70] (see Section
244 2.4). These new larger polygons describe the two-dimensional projection of tree assemblages. Then, as our interest
245 focused on the extent and shape of the tree assemblages, the inner borders of the merged polygons were disregarded.
246 To reduce computation time, the polygon shapes were simplified by reducing the number of vertices and edges to 70 %
247 while keeping the polygon shape.

248 2.4 | Definition of Context Via Tree Neighborhood

249 We determined at what distance neighborhood metrics should be calculated (i.e. how many surrounding trees should
250 be accounted as neighbors) based on local similarity of tree height. Accordingly, the selection of an appropriate
251 neighborhood size around each individual tree (i.e. context detection) [71] was calculated through the analysis of
252 spatial autocorrelation of tree height as function of incremental distance, as in previous studies [72]. Based on the
253 global peak in the significance of spatial autocorrelation, we defined a characteristic distance within which all included

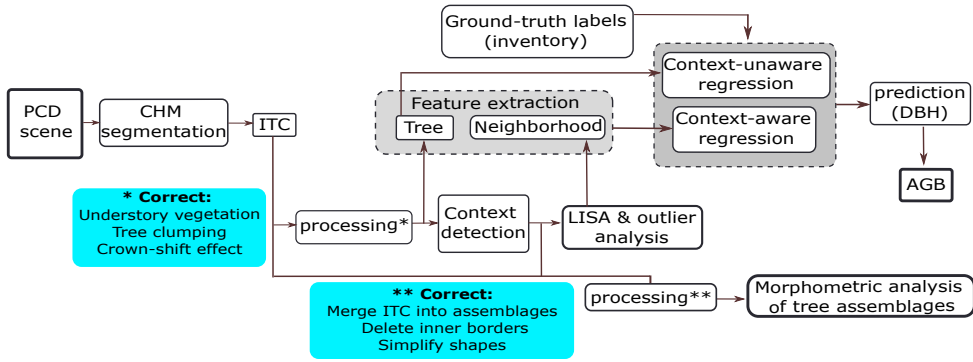


FIGURE 3 Workflow followed in this study. PCD: point cloud data, CHM: canopy height model, ITC: individual tree crown, LISA: local indicators of spatial association, DBH: diameter at breast-height, AGB: aboveground biomass. The two colored boxes describe the subtasks constituting each of the processing steps, marked * and ** in the diagram.

254 trees should be considered as neighbors. Then, all so-defined neighbor trees were accounted for to compute context-
 255 aware metrics.

256 The local context information was encoded as metrics derived from the individual tree heights in each neighbor-
 257 hood, calculated at each tree location. Specifically, the metrics computed to define tree neighborhoods were: local
 258 Moran's I [36] clustering (i.e. an estimate of local significance of similarity with respect to global variance); and (SL_i)
 259 of tree height (i.e. a weighted average of heights calculated entirely locally) [70].

260 2.5 | Neighborhood Information as Predictive Features

261 2.5.1 | Neighborhood Metrics

262 Local Moran's I_i is a well-established distance statistic in spatial data analysis [73], used for detecting local spatial
 263 autocorrelation and included within the family of LISA methods [41]. Like other methods [74], it relates attribute
 264 similarity with locational similarity, mapping autocorrelation across the geographic space. In the following definitions,
 265 σ is the global sample standard deviation of tree height; n and m represent the total number of instances (i.e. all
 266 trees in the forest) and the number of neighbors to each tree, respectively; y_i indicates the magnitude of interest
 267 at a particular point of interest (i.e. tree height) while the overline (i.e. \bar{y}) indicates global average; $w_{i,j}$ indicates the
 268 distance weighting of each neighboring tree (here defined as inverse distance weighting); subindexes i and j indicate
 269 the tree of interest and a neighbor tree, respectively. Let y_1, \dots, y_n be the tree height values of all the n trees in the
 270 dataset. Then, the Local Moran I_i [36] is defined as

$$I_i = \frac{y_i - \bar{y}}{\sigma^2} \sum_{j \in N_i, j \neq i} w_{i,j} (y_j - \bar{y}), \tag{1}$$

271 where $N_i \subset \{1, \dots, n\}$ is the set of indices corresponding to the nearest neighbors of tree $i \in \{1, \dots, n\}$ in the overall
 272 set, with $\sum_{j \in N_i, j \neq i} w_{i,j} = 1$ and where

$$\bar{y} = \frac{1}{n} \sum_{i=1}^n y_i, \quad (2)$$

273 and

$$\sigma = \sqrt{\frac{\sum_{i=1}^n (y_i - \bar{y})^2}{n - 1}}, \quad (3)$$

274 are the global average height and the global sample standard deviation, respectively. It should be noted that insofar
 275 I_i includes global metrics (such as n , σ and \bar{y}), it is not entirely locally computed, but may present correlation with
 276 global features (i.e. characteristics derived from the entire dataset) [75]. The Spatial Lag (SL_i) of tree height for a tree
 277 i is a spatial smoother [76] defined as:

$$SL_i = \sum_{j \in N_i, j \neq i} w_{i,j} y_j \quad (4)$$

278 Therefore, SL_i can be seen as a weighted average of the attributes of neighboring trees [77]. The neighborhood
 279 metrics finally chosen as context-aware predictors are the following: local Moran's Index (I_i), z-score of I_i , p-value of
 280 I_i , z-transformed value of I_i and SL_i - computed at 20 m, 30 m, 40 m and 50 m distance bands. Additionally, the
 281 mean heights of the k-nearest trees, with $k \in (5 - 75)$, were also included.

282 2.5.2 | Environmental Variables

283 We also included the topographic wetness index (TWI) [78] as environmental variable. TWI is a steady state wetness
 284 index used to evaluate topography-dependent surface hydrology processes. According to [78], TWI is defined as
 285 $\frac{a}{\tan(b)}$, where a represents the upslope area draining through the point of interest, and b indicates the local slope. The
 286 parameterization considered to calculate TWI followed the suggestions of Kopecký et al. (2021) [79] for estimating
 287 soil moisture. In order to discern how much the contribution of TWI is influenced by granularity, we calculated it at
 288 a 2 m^2 resolution, and resampled to 5 and 10 m^2 , via bilinear interpolation. Therefore, TWI was included at a spatial
 289 resolution of 2, 5 and 10 m^2 as separate predictors.

290 2.6 | Tree Assemblages: Definition and Morphometry

291 In order to define tree assemblages, local Moran's I_i and SL_i were both computed at the optimal distance band to
 292 obtain neighborhood metrics, i.e. based on the global peak in the significance of spatial autocorrelation as a function
 293 of distance (using ArcGIS Pro software [80]). Tree assemblages were therefore defined as geographically continuous
 294 groups of trees delineated according to either (i) variation of local Moran's I_i of tree height, or (ii) according to quantiles
 295 of SL_i of tree height. The rationale for using two different statistics to calculate tree neighborhood metrics and thus
 296 delineate different tree assemblages was that while SL_i is entirely locally calculated, local Moran's I_i includes global
 297 features (and is therefore sensitive to the statistical characteristics of the dataset as a whole), as explained in Section

298 2.5.1. In order to discern which of the two approaches seemed most convenient in delineating tree assemblages (the
299 former *entirely* local; the latter only *partially* local), both were included.

300 Tree assemblages defined according to local Moran's I_i are geographically continuous groups of trees with signif-
301 icantly different heights than the global tree height average, and they also lie in a region with significantly different
302 neighbors. Local Moran's I_i identifies regions where the clustering of either high or short trees occurs. In the standard
303 notation [70] (i.e. *High-High* or *Low-Low*), the first term refers to the individual tree and the second to the neighborhood
304 (e.g. a tree belonging to a *High-High* assemblage is a "significantly high tree" in a "significantly high neighborhood").
305 The areas not showing statistical significance (p-value ≥ 0.002) were labeled as *Not-Significant*. The significance test is
306 based on random permutations (n = 499) of neighboring tree-height values at each step in the computation. The num-
307 ber of permutations and p-value indicate that, under the null hypothesis (i.e. tree heights being randomly distributed),
308 a single tree canopy is likely to be wrongly classified with a probability of 0.002, which was deemed sufficient for the
309 purpose of evaluating tree neighborhood shapes (i.e. if 1 out of 499 trees is wrongly attributed to a neighborhood,
310 the morphometry of the neighborhood will not change significantly). Then, for every permutation, a local Moran's I_i
311 value is calculated by randomly rearranging the tree heights of neighboring values. The result is a randomly gener-
312 ated reference distribution of expected local Moran's I_i that is compared against the observed local Moran's I_i (Eq.
313 1) [41]. In this way, tree assemblages defined according to local Moran's I_i are classified as: *High-High*, *Low-Low*, or
314 *Not-Significant*.

315 Likewise, tree assemblages defined according to SL_i of tree height are geographically continuous groups of trees
316 delimited according to the local weighted average of tree height [77], as defined above (Eq. 4). For the purpose of
317 this study, 5 subdivisions based on quantiles were deemed convenient, rendering a classification of tree assemblages
318 based on SL_i ranking as: *Highest*, *High*, *Mid*, *Low* and *Lowest*.

319 The morphometric analysis used as its objects of analysis the outer boundaries of tree assemblages, defined
320 either by local Moran's I_i or SL_i of tree height, as defined above. Twenty basic morphometric parameters as well
321 as 20 derived parameters were calculated for each type of tree assemblage. The 20 basic morphometric variables
322 are simple parameters obtained by fitting elemental geometric shapes to each tree assemblage polygon (e.g. area
323 of maximum inscribed circle), and basic positional parameters (e.g. XPOL, which is the X coordinate of the centroid
324 of the tree assemblage polygon). The 20 derived parameters are adimensional metrics (except for concavity [81],
325 measured in m) computed from the 20 basic morphometric variables, as explained in [82] (a full description of the 40
326 morphometric parameters is given in Annex I). The morphometric analysis of tree assemblages was conducted using
327 PolyMorph-2D algorithm [82], which is a toolbox for the morphometric analysis of vector-based polygon objects,
328 available as a plug-in for the open source JumpGIS software [83].

329 2.7 | Regression Models Selected

330 The regression experiments were designed to predict DBH, since AGB is a variable determined by the combination of
331 DBH, height and wood density. The AGB estimates were derived from the DBH prediction outputs by means of an
332 allometric fit (Eq. 5). Predicting DBH, instead of AGB directly was chosen as more suitable, as it avoids burdening the
333 learning models with the statistical error contained in the allometric fit. Several feature-based regression methods
334 were selected: namely AdaBoost [84, 85], Lasso [86] and Random Forest [87] regressors.

335 The AdaBoost regressor [88] is a gradient-boosting method based on stage-wise additive expansions; its effec-
336 tiveness rests on the combination of weak learners (i.e. decision trees) to produce a generalized prediction hypothesis.
337 Lasso is a linear model with $L1$ prior penalty as a regularizer [89], while Random Forest is a tree-based ensemble re-
338 gression method. In our case, all three feature-based methods take as input the features derived from the ITC polygon

dataset resulting from the CHM segmentation.

Context-unaware regressions are defined as those in which a learning model performs DBH regression by taking as predictors only individual tree attributes derived from the ITC polygon dataset (i.e. tree height, canopy area and canopy perimeter), as it is a common approach [19]. We defined context-aware regressions as those regressions in which context-aware features are additionally introduced as input. These come in the form of either neighborhood metrics, e.g. SL_i of tree height, or as environmental variables, i.e. TWI at different spatial resolutions. Both the neighborhood metrics and environmental variables used are described in Section 2.5.1 and Section 2.5.2, respectively. For every model predicting DBH from individual tree attributes (i.e. context-unaware conditions) we implemented a context-aware counterpart.

2.8 | Training, Validation and Test

A hard validation of AGB is not possible without harvesting trees destructively, which raises obvious ethical, legal and economic issues. Thus, non-invasive methods that use RS data and allometric functions are the standard procedure for estimating AGB [90]. Here, we estimated AGB from tree height, DBH and an allometric function (eq. 5). The regression analyses conducted are focused on comparing performance of predictions on DBH between models (i) "unaware of context" and their (ii) "context-aware" counterparts.

We chose DBH as the variable to test model predictions, which is a tree morphological trait contained in the field-based forest inventory, and therefore directly measured by *in situ* monitoring. Next, in order to assess the benefits of including context in the regression models, we compared results using AGB of individual trees. Hence, AGB estimates were derived via species-specific allometric and wood density functions, tree height retrieved via UAV-LiDAR, and DBH predicted via ML regression. Specifically, the allometric model used was the one proposed by Dalponte and Coomes (2016) [91]:

$$AGB_{tree} = \alpha \cdot WD_{spruce}^{\beta} \cdot (DBH - d_0)^{\gamma} \cdot H^{\delta}, \quad (5)$$

where the wood density value (WD_{spruce}) was taken from Alpine spruce dendrometric models [92], diameter at breast-height (DBH) was predicted via ML regression and height (H) was extracted from the UAV-LiDAR data. $\alpha, \beta, \gamma, \delta$ and d_0 are species-specific fitted allometric parameters [93], obtained from allometric fits to harvested spruce trees by the Forestry and Wildlife Service Agency of the province of Trento (Italy, 150 km southeast from the study site, also used by Dalponte and Coomes [91]), and we consider them applicable to the Seehornwald Davos research site. At all events, for the purpose of assessing the benefits of a context-aware approach, the specific characteristics of the allometric fit used are negligible, as it is only used to quantify a difference in terms of AGB, and both types of predictions (unaware and aware) take the same equation.

Hence, the AGB assessment was derived from the predictions of DBH (and LiDAR-derived height) in either aware or unaware conditions. Therefore, the predicted value of DBH was input into Eq. 5, in order to obtain predictions of AGB. This allowed to compare AGB predictions to the ground-truth values of AGB, which were similarly obtained via the field-based measurements (provided by the regular tree-monitoring campaigns of ICOS [58] and WSL [55]) and Eq. 5.

For training and validating the regression models, the instances with empty ground-truth labels were initially removed (i.e. trees with no DBH or tree height recorded). Afterwards, data stratification was done via five commonly used percentiles (i.e. 0-10, 10-25, 25-50, 50-75, 75-90, 90-100) to ensure that input data is independently drawn

376 from an identical sample distribution (i.i.d. assumption) [94]. This assured us that most parts of the target distribution
 377 are represented, in particular the tail ends. Then, the technique used to estimate model prediction error consisted of
 378 a nested cross-validation (NCV) [95]. Following the NCV scheme, we divided the input dataset (either CP, or SP, corre-
 379 spondingly) into 10 inner and 10 outer folds. The inner cross-validation was used for hyperparameter optimization and
 380 feature selection, while the outer cross-validation was used to evaluate model performance (the method description
 381 is extended in Section 4.4 and further details are given in Annex III). The significance of the enhancement in context-
 382 aware predictions and effect size was assessed using Wilcoxon signed-rank test [96] and Cliff's Delta analysis [97],
 383 respectively.

384 3 | RESULTS

385 3.1 | Context Detection and Tree Assemblage

386 The analysis of spatial autocorrelation of tree height as function of incremental distance resulted in a maximum sig-
 387 nificance at a distance of 40 m. Figure 4 (a) shows the calculation of local Moran's index (I_i) of tree height at different
 388 distance bands. Figure 4 (b) shows the z-score of I_i , obtained at each distance band, resulting from comparing the
 389 observed I_i and the expected I_i under the tree height randomness assumption (details included in the Annex II). As
 390 a sanity check, we ran context-aware regression experiments including context features retrieved at shorter (i.e. 20
 391 m, 30 m) and larger (i.e. 50 m) distances than the optimal range (i.e. 40 m). The context features retrieved at these
 392 distances and that contributed to improved predictions of DBH were also included in the final regression models.

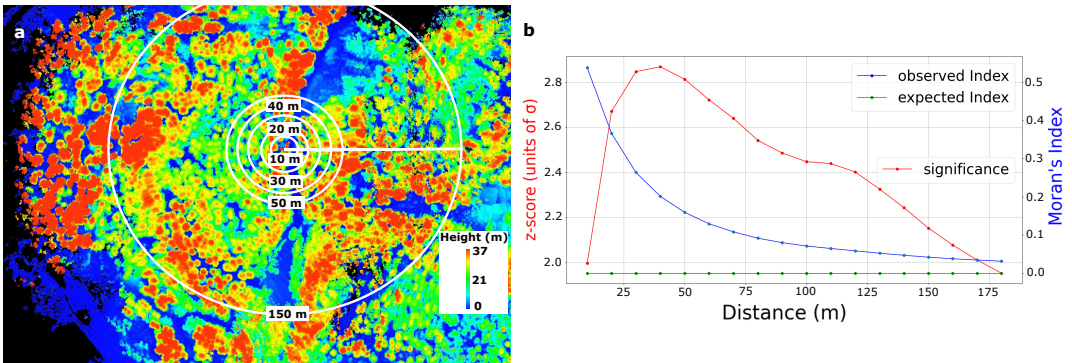


FIGURE 4 Context detection. **a:** normalized point cloud data (PCD) scene colored by tree height overlaid with a selection of the appropriate radii for defining the neighboring context. **b:** Autocorrelation of tree height as function of distance. The red line shows the number of standard deviations (σ) that an observation is away from the expected value (under the assumption of heights being randomly distributed). The blue and green lines show the actually observed local Moran's Index and the expected value under randomness assumption, respectively.

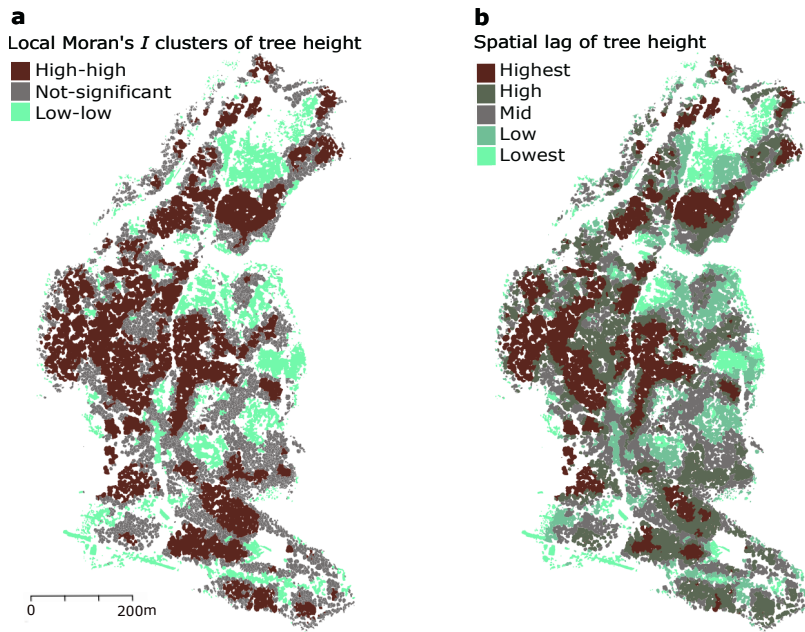


FIGURE 5 Tree assemblages defined by local similarity of tree height. **a**: delineated according to local Moran's I_i of tree height; **b**: delineated according to spatial lag of tree height.

393 Figure 5, a and b, show the spatial distribution of different tree assemblages defined by local Moran's I_i and by
 394 SL_i of tree height respectively. While both types of assemblages show similarities as regards extent and location,
 395 SL_i captures more local variability. This is not only due to a higher discretization (5 groups in SL_i , vs. 3 groups in
 396 local Moran's I_i), but also to the fact that SL_i is insensitive to the variance in the dataset beyond the range of its
 397 neighborhood, as explained in Section 2.5.1 (in Figure 5, both assemblage types shown were derived from these two
 398 metrics, calculated at 40 m range).

399 Figure 6, panels a and b, show the results of the morphometry analysis of tree assemblages defined by local
 400 Moran's I_i and by SL_i respectively. The results are based on the shape of the outer contours of the resulting tree
 401 assemblages. The circular barplots show the average magnitude as bar lengths, and the standard deviation as dots.
 402 Both mean and standard deviation values are shown as min-max scaled (across assemblage types) to present all vari-
 403 ables on the same radial axis and to ease visual comparison, i.e. for every morphometric variable, the highest value is
 404 replaced by 1, the minimum is replaced by 0, and the intermediate values are linearly interpolated between 0-1.

405 While not for all variables a systematic trend was found, for several basic morphometric variables a linear positive
 406 correlation between them and SL_i was observed, as shown by the Pearson coefficient. This is the case for polygon
 407 area ($\rho=0.95$), perimeter of polygon (PPOL; $\rho=0.98$) and radius of the minimum circumscribed circle (RMCC; $\rho=0.98$).
 408 Additionally, a positive correlation was found for some derived morphometric variables, namely: length-to-width ratio
 409 (LTWR; $\rho=0.75$) [98], circularity ratio (CIRR; $\rho=0.88$) [101], compactness factor (COMF; $\rho=0.89$) [82], dispersion mea-
 410 sure (DISM; $\rho=0.90$) [101], complexity index (COMI; $\rho=COMI$) [82], lemniscate ratio (LEMR; $\rho=0.81$) [105], regularity
 411 factor (REGF; $\rho=0.82$) [100], and concavity (CONC; $\rho=0.96$) [81]. Conversely, other morphometric variables showed
 412 a decreasing trend with increasing SL_i . A negative correlation between SL_i and the following derived morphome-
 413 tric variables was found: Miller's circularity ratio (MCIR; $\rho=-0.88$) [103], Horton's form factor (HFOR; $\rho=-0.88$) [98],

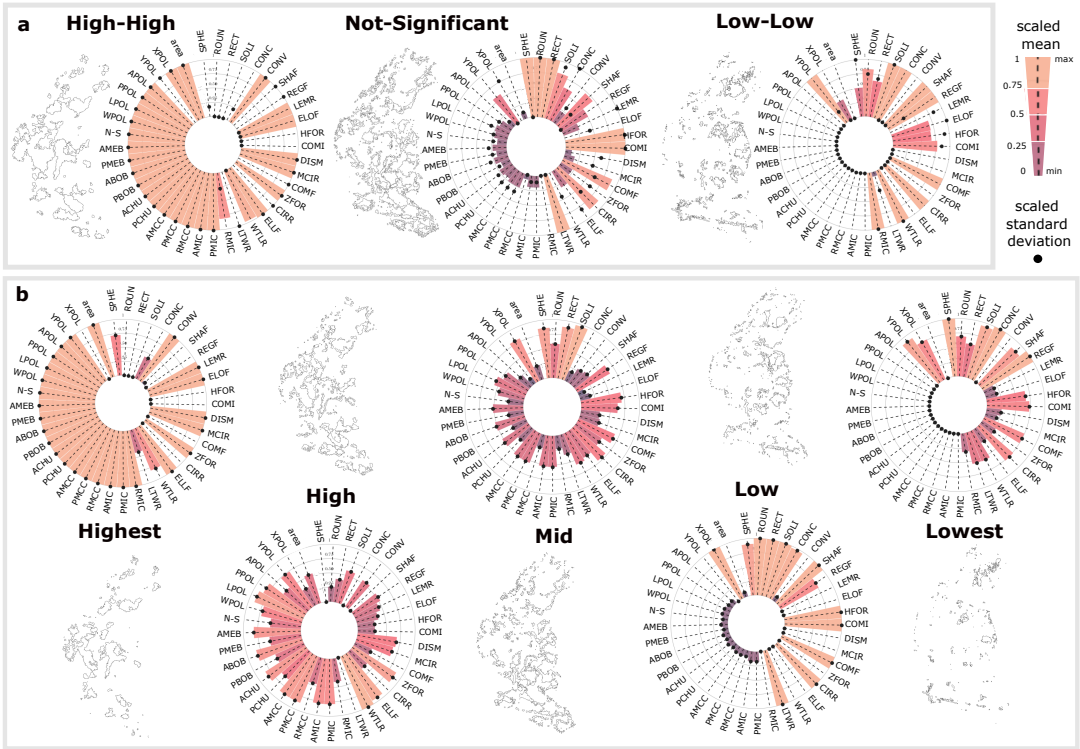


FIGURE 6 Morphometric analysis of tree assemblages grouped by (a) local Moran's I_i , and (b) by spatial lag of tree height. Bar length and color gradient represent the mean value, while black dots represent the standard deviation (SD) over all tree assemblages. Both mean and SD are scaled (min-max) to allow comparison of all metrics across assemblage types on the same axis—i.e. for every morphometric variable, the highest value of a certain assemblage type is replaced by 1, the minimum value is replaced by 0, and the intermediate values are linearly interpolated in between the range (0-1). YPOL: northing of centroid of the tree assemblage; XPOL: easting of centroid of the assemblage; APOL: area of polygon (P); N-S: defined as $|\sin(\text{azimuth})|$, shows the alignment of the main axis of P with the North-South direction; PPOL: perimeter of P; LPOL: major axis length (L) of P; WPOL: minor axis length (W) of P; ABOB: area of the bounding box fully containing P; PBOB: perimeter the bounding box fully containing P; AMEB: area of the minimum enclosing box fully containing P; PMEB: perimeter of the minimum enclosing box fully containing P; ACHU: area of containing hull; PCHU: perimeter of convex hull fully containing P; AMCC: area of the minimum circumscribed circle (MCC); PMCC: perimeter of MCC; RMCC: radius of MCC; AMIC: area of maximum inscribed circle (MIC); PMIC: perimeter of MIC; perimeter of MCC; RMIC: radius of MCC; LTWR: length-to-width ratio [98]; WTLR: width-to-length ratio [99]; ELLF: ellipticity factor [100]; CIRR: circularity ratio [101]; ZFOR: Zavoianu's form factor [102]; COMF: compactness factor [82]; MCIR: Miller's circularity ratio [103]; DISM: dispersion measure [101]; COMI: complexity index [82]; HFOR: Horton's form factor [98]; ELOF: elongation ratio [104]; LEMR: lemniscate ratio [105]; REGF: regularity factor [100]; SHAF: shape factor [100]; CONV: convexity [106]; CONC: concavity [81]; SOLI: solidity [107]; RECT: rectangularity [108]; ROUN: roundness [106]; SPHE: sphericity [109].

414 elongation factor (ELOF; $\rho=-0.83$) [104], shape factor (SHAF; $\rho=-0.95$) [100], rectangularity (RECT; $\rho=-0.85$) [108] and
 415 roundness (ROUN; $\rho=-0.69$) [106].

416 It can be observed (Figure 6) that the morphometric variables follow very similar trends when tree assemblages

417 are defined based on local Moran's I_i or SL_i . However, an observed difference between SL_i and local Moran's I_i was
 418 found in the heteroscedasticity of the morphometric variables calculated. In the former case, we observed that the
 419 variance of all metrics scaled with magnitude (i.e. constantly increasing variance), while in the latter an irregular trend
 420 was found (i.e. an uneven trend in the variance). We visualized these observations in the distribution of scaled mean
 421 values and scaled standard deviations in Figure 6, a and b.

422 3.2 | AGB Predictions: Aware vs. Unaware of Local Context

423 Regression experiments including context-aware features improved predictions of DBH consistently (see Tables 1
 424 and 2), resulting in spatially resolved enhanced tree-level AGB predictions via allometry (Eq. 5). Although consistent,
 425 the degree of prediction enhancement differed between both datasets considered. Predictions in the CP-dataset
 426 observed a lower enhancement in comparison to predictions in the SP-dataset. For instance, RMSE was reduced
 427 by 9.1% (SP-dataset) vs. 4.0% (CP-dataset), and R^2 increased by 3.5% (SP-dataset) vs. 3.2% (CP-dataset). This was
 428 expected, due to less variability in context in the CP-dataset.

429 In Figure 7, the left panel (a) shows the ground-truth labels (i.e. field based estimates of AGB), which were derived
 430 from the field measurements and a species-specific allometric fit (i.e. Eq. 5). The central panel (b) shows the spatial
 431 distribution of residuals (i.e. $e = AGB_{ground-truth} - AGB_{prediction}$) of the AdaBoost context-aware regression results.
 432 The mean values converge towards zero (i.e. $\bar{e}_{SP} = 3.8$ kg, $\bar{e}_{CP} = -3.2$ kg), while the spread of the error distribution
 433 varies between SP and CP datasets (i.e. $\sigma(\epsilon_{SP}) = 123$ kg, $\sigma(\epsilon_{CP}) = 140$ kg).

434 The lack of high spatial autocorrelation of errors (i.e. low clustering of errors) indicates that predictions are not
 435 geographically biased. The upper-right panel (c) displays the error distributions in both datasets. SP-errors show a
 436 unimodal distribution with a slight overestimation of DBH of -28 mm (i.e. overestimation). CP-errors present a similar
 437 overestimation bias (-25 mm) with a bimodal distribution (the second mode is located at 25 mm of underestimation).
 438 The second mode of the bimodal pattern in the CP dataset (at 25 mm) may correspond to the more frequent occurrence
 439 of larger trees, which tend to be underestimated (Figure 7, c, lower panels). The two bottom-right panels show the
 440 error distribution of DBH predictions along the ground-truth measurements of DBH and tree height, respectively.
 441 It can be observed that, generally, smaller and thinner trees tend to be slightly overestimated (i.e. in the first two
 442 quantiles), while the largest trees (i.e. quantile 5 and highest trees) tend to underestimation.

443 Figure 8 presents the analysis of the relative importance of all predictors considered in the context-aware DBH
 444 regression with the AdaBoost regression model (i.e. the best performing one). The analysis reveals that in both SP
 445 and CP datasets, the most important context-based predictors are the average heights of the 5, 10, and 15 nearest
 446 neighboring trees, outperforming some individual-tree metrics, such as the crown metrics.

TABLE 1 Results (on test set) of the sampling plot (SP) dataset. Predictor variables are LiDAR-derived features; target variable is diameter at breast-height (DBH, in mm). The values are presented as mean ± standard deviation of the 10 outer CV folds. One asterisk (*) marks results where the enhancement introduced by context-awareness is statistically significant with "small" size effect, while ** and *** mark "medium" and "large" size effect, respectively. The best results are shown in bold.

Regression model	R ²	RMSE (mm)	MAE (mm)	MAPE (%)
AdaBoost (unaware)	0.830 ± 0.05	58.0 ± 9.0	43.3 ± 4.4	19.1 ± 1.9
AdaBoost (aware)	0.860 ± 0.03 ***	52.7 ± 5.3 ***	41.0 ± 3.1 **	19.5 ± 1.7
Random Forest (unaware)	0.818 ± 0.04	60.2 ± 7.3	46.8 ± 4.5	22.8 ± 5.8
Random Forest (aware)	0.838 ± 0.05 *	56.5 ± 9.2 *	41.6 ± 5.4 ***	22.4 ± 5.1
Lasso (unaware)	0.851 ± 0.02	54.6 ± 4.9	4.20 ± 3.3	19.1 ± 1.4
Lasso (aware)	0.852 ± 0.02	54.4 ± 4.9	4.17 ± 3.5	18.8 ± 1.7

TABLE 2 Results (on test set) of the control plot (CP) dataset. The predictive variables are LiDAR-derived features; the target variable is diameter at breast-height (DBH, in mm). The values are presented as mean ± standard deviation of the 10 outer CV folds. One asterisk (*) marks results where the enhancement introduced by context-awareness is statistically significant with "small" size effect. The best results are shown in bold.

Regression model	R ²	RMSE (mm)	MAE (mm)	MAPE (%)
AdaBoost (unaware)	0.713 ± 0.07	54.7 ± 5.98	43.0 ± 5.26	15.5 ± 2.4
AdaBoost (aware)	0.737 ± 0.05 *	52.9 ± 5.28 *	42.2 ± 4.43 *	15.7 ± 3.1
Random Forest (unaware)	0.688 ± 0.07	57.0 ± 5.9	43.8 ± 5.1	15.7 ± 3.1
Random Forest (aware)	0.705 ± 0.04	55.6 ± 5.3	41.3 ± 5.5 *	15.9 ± 4.3
Lasso (unaware)	0.741 ± 0.09	51.3 ± 6.6	39.1 ± 5.2	13.6 ± 1.6
Lasso (aware)	0.750 ± 0.08	50.4 ± 5.9	38.6 ± 4.1	13.6 ± 1.1

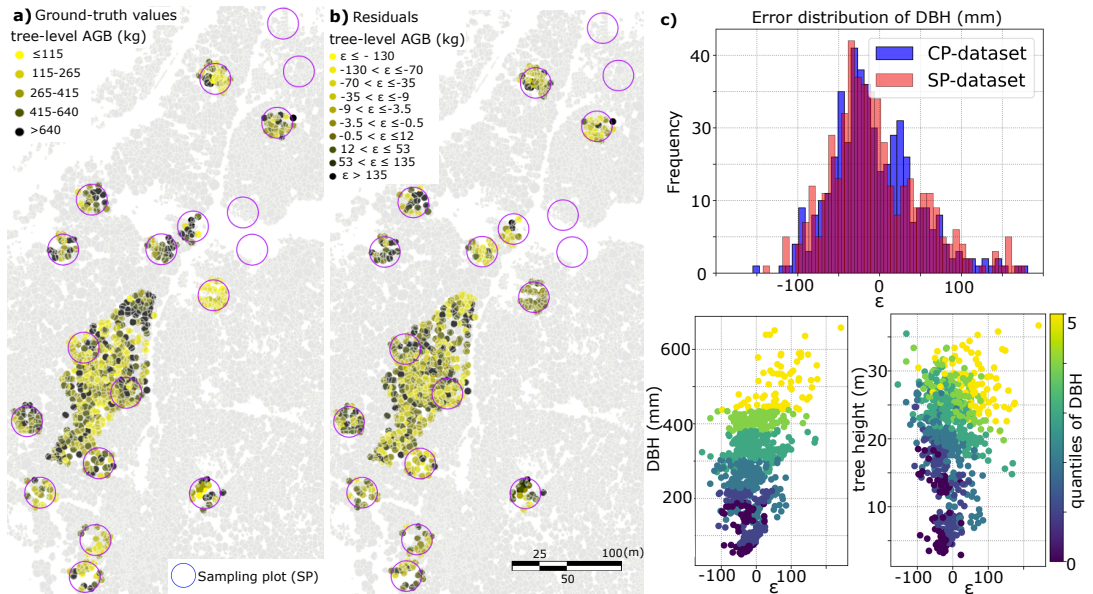


FIGURE 7 a: spatial distribution of tree-level aboveground biomass (AGB) according to ground-truth measurements (provided by the tree-monitoring campaigns of ICOS [58] and WSL [55]) and Eq. 5, grouped by quantiles. b: spatial distribution of residuals ($\epsilon = AGB_{ground-truth} - AGB_{prediction}$) of AGB predictions with AdaBoost context-aware regression, grouped by quantiles. Negative values indicate overestimation. The four empty SP-plots (and the southernmost one not included) correspond to areas where the quality of the UAV-LiDAR data collection was compromised; in such five plots, due to high level of noise in the point cloud data, all data were rejected. c: error distributions of diameter at breast-height (DBH) in sampling plot (SP) and control plot (CP) datasets. The two bottom-right panels show the error distribution of DBH (in x-axis) vs. field-measurements of DBH and tree height. Colors do not entirely show a clear separation (especially below 200 mm DBH) because the quantiles refer to each dataset separately, which are differently distributed, as it is shown in Annex IV.

448 4 | DISCUSSION

449 4.1 | Enhancement of Tree-Level AGB Prediction

450 This study presents a method of enhancing tree-level AGB estimates in forests using UAV-LiDAR surveying and
 451 context-aware ML regression methods. The results consistently showed that context-aware regressions outperformed
 452 context-unaware regressions across models (except for Lasso in SP-dataset, where performance stagnates). This
 453 finding indicates that gradients in morphological tree traits across the ecosystem may be a proxy for unveiled en-
 454 vironmental and biotic factors (e.g. windstorm disturbance, nutrient and soil moisture abundance, light harvesting
 455 competition) [37, 38] that influence tree growth, which can be leveraged to enhance predictions of AGB.

456 The accuracy enhancement gained from including context-aware features in the regression experiments varied
 457 between the two datasets considered (i.e. SP-trees and CP-trees). Context-aware regressions of DBH in SP-trees
 458 experienced greater enhancement than CP-trees. This is consistent with the fact that the CP-dataset contains less
 459 variability of context, since it is a clustered and more homogeneous dataset, while the SP-dataset includes more
 460 variability in context-aware features. The investigated spruce forest presents a heterogeneous landscape, where the
 461 distribution of tree heights varies in space. Hence, the UAV-LiDAR survey gives rise to a non-stationary tree dataset

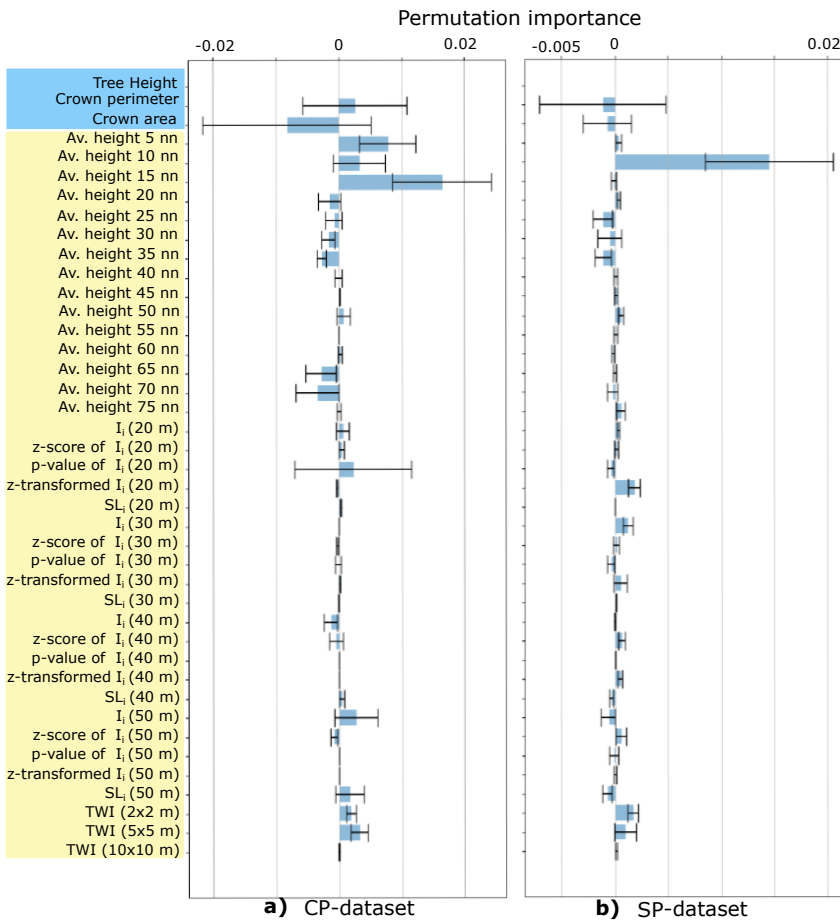


FIGURE 8 Inspection of predictors' importance via the permutation method [110] in AdaBoost regression experiment in context-aware conditions. The left panel (a) shows results in the control plot (CP)-dataset, and the right panel (b) shows results in the sampling plot (SP)-dataset. Bar length and error bar show the mean and standard deviation of a predictor's importance, respectively. A negative mean value indicates that a predictor is less useful than when being randomly shuffled, so it lowers the model's predicting performance. Predictors highlighted in light blue are individual tree traits; predictors highlighted in light yellow are context-based (i.e. either neighborhood metrics or environmental variables). In both datasets, it can be noted how the average heights of the nearest neighbors (nn) stand out as the strongest context-based predictors. In both plots (a and b), individual tree height (with importance: 0.85 in CP-trees; 1.3 in SP-trees) has been removed to ease visual comparison of the remaining predictors.

462 [71], showing both smooth gradients and sharp changes in height values, a non-trivial question in tree-phenotyping
 463 and species mapping [43]. As SP-trees are grouped in scattered plots across the forest, their spatial distribution spans
 464 hundreds of meters, making them subject to a more diverse context than the very local CP-dataset.

4.2 | The Role of Neighboring Context in AGB Prediction Performance

All regression models achieved enhanced predictions when contextual information was considered. Thereby, the degree of local similarity of tree height (i.e. SL_i , local Moran's I_i) was most important and, to a lesser extent, environmental variables (i.e. TWI).

Conversely, including features informing about neighbor dissimilarity, such as local outliers detected using Local Outlier Factor [68] and Isolation Forest [69] algorithms did not result in enhanced predictions. We hypothesize that metrics containing information about the degree of local similarity may reveal the combined effect of ecological processes that are specific to the immediate neighboring context. Conversely, metrics containing information of the dissimilarities of the individual trees do not help to uncover such processes, but remain useful in detecting outstanding trees (i.e. local outliers).

Context-based features at closer distances generally showed larger predictive power but also larger variance (as less neighboring trees are computed), therefore producing a strong and fluctuating signal, that in some cases was challenging for the ML model to incorporate in the learning process. For instance, the p-value of Local Moran's I_i at a 20 m range in the CP-dataset has an average positive effect but is not a stable predictor (Figure 8, a). This can be observed in the general trend of larger standard deviations in the permutation importance of predictors retrieved at short ranges than at greater distances (Figure 8). After the peak in the spatial autocorrelation of tree height (i.e. at larger distance bands than 40 m), the significance of clustering of tree height values declined, presenting another shoulder at a distance of 110 m (Figure 4, b). As the neighborhood size increased beyond the 40-meter distance range, the predictive power of the metrics derived from the neighboring trees (i.e. the influence of local context) progressively smoothed down [76].

In accordance with competition-based studies [23, 24, 25], we observe that the strongest context-based predictors are those retrieved from the immediate neighboring trees in both datasets, i.e. the average height of 5, 10 and 15 nearest neighbors (Figure 8). This observation indicates that individual tree structural traits are primarily mediated by competition mechanisms. However, our method additionally allows to compare the relative importance of competition-derived metrics and other context-based metrics operating at larger scales. For instance, in Figure 8 (a) it is shown that local Moran's I_i retrieved at a 50 m range is comparable in importance to the average height of the closest 10 neighboring trees.

A general difference observed between the CP and the SP dataset is that the predictors' importances in the CP-dataset fluctuate more (i.e. larger standard deviations). Further, in the SP-dataset, predictors rarely become negative and if they do, it is to a lesser extent. Given its broader spatial distribution and greater contextual variability, we contend that the SP-dataset can be regarded as a more representative sample of the entire forest population compared to the clustered CP-dataset. Consequently, the finding that context-based features demonstrate greater stability within the SP-dataset is noteworthy.

In relation to the environmental metrics used, TWI exhibited a greater impact on improved predictive performance at finer spatial resolutions in both datasets (Figure 8), whereas its contribution decreased at coarser resolutions (e.g. it did not significantly contribute as a predictor at 10 m resolution). This observation indicates that the spatial resolution at which TWI is most informative of individual tree traits, is similar to the usual tree crown size (i.e. 2-5 m resolution), while at larger scales its contribution as predictor becomes negligible.

The morphometric analysis (Figure 6, a and b) provided 40 additional features that were evaluated as potential predictors of DBH. However, including morphometric variables calculated from the tree assemblages in the regression experiments—either defined by SL_i or by local Moran's I_i —did not result in improved predictions of DBH. As shown in Figure 5, the shape of tree assemblages shows sensitivity to the method used. The shapes of tree assemblages showed

507 certain convergence assembly patterns [111], as discussed in Section 4.3. Nevertheless, the group morphometry did
508 not prove useful to improve predictions of DBH.

509 Including context to enhance estimates of structural traits at the individual tree level has previously been pro-
510 posed in seminal works [27] and been adopted subsequently for various applications in forest research [26, 28]. Lo
511 and Lin (2012) [25] proposed a competition-specific index to capture the effect of the competing pressure of imme-
512 diate neighbors. More recent research conducted in this area [23, 24] has motivated the further development of
513 competition-aware approaches to improve the prediction accuracy of individual tree traits, using overstory tree traits
514 as predictors, such as tree height and crown metrics, which enables the potential transferability of these methods to
515 a fully integrated RS framework.

516 In forest biomass research, a commonly recognized approach is calibrating regression models with plot-level met-
517 rics for predicting tree-level structural traits (e.g. parameters accounting for plot-level random effects in NLME meth-
518 ods). However, such approaches do not question the influence of the artificially-delineated plot size on prediction
519 enhancement, even if it is observed that accuracy increases with plot width and number of tree neighbors [20, 22].
520 Furthermore, how diverse context-based attributes retrieved at different distance ranges affect tree-level predictions
521 had not been investigated before. In this regard, our results show that the variability and extent of context determines
522 its beneficial leverage for prediction of tree-level traits (e.g. DBH, AGB).

523 Our study continues this line of work and sheds light on how the local spatial context can be defined and leveraged
524 in tree-level structural trait predictions (i.e. DBH), making a case for AGB estimates. The analysis shows that there is
525 an optimal range to computing neighborhood metrics. In the case of the spruce forest studied here, this corresponded
526 to a 40 m range distance, based on the spatial autocorrelation of tree heights. Further, we found that the predictive
527 power of context-based metrics is sensitive to context extent (i.e. the distance at which such metrics are calculated).
528 This observation indicates that considering context based on plot-level metrics retrieved from artificially bounded
529 units (plot-level metrics, as in [20, 21, 22]) may be seen as a suboptimal approach [112]. Likewise, in the light of
530 this observation, and in line with recent studies [113], determining the significant contextual extent of individual
531 functional traits based on fixed pixel-size [114] appears to be a subpar technique. Therefore, future forest research
532 would probably benefit from including context-awareness determined by spatial association of tree traits, bearing in
533 mind that context-detection is trait-dependent and may vary depending on dataset source (e.g. spatial autocorrelation
534 as a function of distance is sensitive to CHM segmentation quality) and method applied (e.g. delineation of tree
535 assemblages varied slightly between local Moran's I_i , and SL_i , as we show in Figure 5, a and b). The motivation for
536 our study has been to introduce more quantifiable terms to ecological reasoning and to propose a standardized method
537 of incorporating context-awareness into AGB research. The method proposed is conceived for a fully integrated RS
538 framework. Since we do not make use of external data sources but, on the contrary, every predictor is native to the
539 UAV-LiDAR dataset, and we do not use understory vegetation metrics, the method may be readily transferable.

540 Lastly, we note that RS studies usually define the optimal scale of analysis as a trade-off between the observational
541 extent (i.e. area surveyed) and the unit resolution (i.e. pixel size) [113]. Also, in ecological research, it is common
542 to subsample datasets using natural subregions based on ancillary ecological criteria (i.e. ecoregions, conservation
543 status) [12]. Conversely, here we defined the range of influence of context-based metrics (i.e. the boundaries of
544 tree neighborhoods) using a dataset-native approach, based entirely on the spatial association of individual tree traits.
545 This permitted us to determine the context of influence unhampered by the RS technique and not using external
546 data sources. In computer vision studies that investigate contextual learning, image analyses typically do not assume
547 a specific optimal scale [115, 116], such as in geographic analysis [117]. In this study, local context was defined
548 based on the spatial association of a real physical attribute of the target objects (i.e. tree height), and not defined
549 by an artificially bounded unit (e.g. pixel size [114] or plot size) so that the resulting distance could be considered

550 informative of the forest ecosystem.

551 4.3 | Tree Assemblages

552 The quantitative comparison of morphometric variables between tree assemblages (Figure 6) permitted to examine
553 whether trees—grouped by local association of an individual trait—persistently show different shapes at the group
554 level, shedding light on the relationship between context-based traits and individual tree traits. Remarkably, it was
555 observed that tree assemblages delineated according to the weighted average of individual tree heights (i.e. SL_i)
556 presented positive correlations with two-dimensional morphometric features at the group level.

557 For instance, assemblages with higher trees (i.e. labeled as *Highest* according to SL_i , or *High-High* according to
558 local Moran's I_i) are consistently rounder, larger and more regular in shape. As visualized in Figure 6, SL_i correlates
559 positively with shape regularity [100], two-dimensional concavity [81], length-to-width ratio [98] and size, indicating
560 a consistent trait-convergence assembly pattern [111]. Higher trees seem to converge in most sheltered areas (i.e.
561 thalwegs and local sub-basins) so that tree assemblages with highest SL_i tend to adopt the morphological features of
562 the drainage network's shape (see Figure 9, in Annex I). Interpretation of this observation would go beyond the scope
563 of this study. However, it may indicate that both the shape and location of tree assemblages of different heights are
564 conditioned by underlying environmental and biotic driving mechanisms.

565 In the spruce forest studied here, tree height clustering occurs (Figure 5, a), while spatial gradients of averaged tree
566 height present preferential shapes and directions (Figure 5, b). These observations indicate that there is tree-height
567 convergence and a tendency toward optimal phenotype expression (i.e. maximum growth performance) around the
568 runoff drainage network (Figure 9, c, in Annex I). Higher trees are found in sheltered regions and concave channels—
569 which generally benefit from more frequent runoff events and deeper soils [39, 40]. This may indicate that favorable
570 environmental conditions (e.g. deeper soil, lower soil moisture-recession rates, greater availability of soil nutrients
571 due to leaching) allow individuals to reach their optimal phenotype. Conversely, a lower SL_i of tree height in more
572 exposed terrain (e.g. ridges, hilltops) indicates that environmental filtering (e.g. windstorm disturbance) or a reduced
573 competition in light harvesting could play a significant role in determining the location of low SL_i tree assemblages
574 (Figure 9, a, in Annex I). Thus, the relatively reduced tree height in exposed areas could indicate a passive response of
575 tree height to harsher environmental conditions [42], an active response to higher light availability [37] or a limitation
576 to tree growth caused by other local factors, such as lower soil depth or nutrients availability [1, 40]. Nevertheless,
577 this study cannot provide an interpretation of such observations, as shifts in the variance of functional traits across
578 environmental gradients (i.e. spatial patterns of trait similarity) do not bring strong evidence of either biotic or envi-
579 ronmental filtering on their own [118].

580 4.4 | Methods Applied

581 The regression methods used (i.e. AdaBoost, Lasso and Random Forest regressors) are well-known methods that take
582 as input features extracted from the polygon dataset obtained after CHM segmentation, abstracted from their spatial
583 location (see Figure 3).

584 The NCV technique [95], used for model optimization and evaluation, follows the updated, most established
585 recommendations to achieve an unbiased estimate of the generalization error, while making optimal use of the limited
586 available data. The results in the inner folds report on training performance, as they are used for model optimization,
587 while the mean performance on the outer folds is the one used for model evaluation. As a modification developed
588 from standard cross-validation [119], NCV improves estimates of prediction accuracy and confidence intervals by

589 accounting for the correlation between error estimates in different folds, an inconvenient phenomenon affecting
590 standard cross-validation that may render error estimates overly optimistic (further details of how the NCV algorithm
591 is implemented are given in Annex III).

592 The inspection technique used to evaluate predictors' influence on the DBH regression results was the permu-
593 tation importance method as proposed by Altmann et al. (2010) [110]. The feature-elimination procedure consisted
594 of eliminating progressively those predictors that presented a negative mean importance, as they were considered
595 harmful to the model's performance.

596 In order to evaluate the statistical significance of the enhancement introduced by context-awareness, we used
597 the Wilcoxon signed-rank test [96], while for the assessment of effect size we used the Cliff's Delta analysis [97].
598 These two tests were conducted in the same 10 outer folds of the NCV routine (i.e. test data) in aware and unaware
599 conditions, so that results were compared using the exact same test data folds.

600 One constraint we acknowledge is that the strength of these results is limited by not having replicated the study
601 at different forest sites. This makes it challenging to readily consider these findings generally applicable to a wider
602 range of forest types. Therefore, further research is needed to validate and extend these findings across various
603 geographical contexts and forest ecosystems.

604 5 | CONCLUSIONS

605 This study is the first to introduce and evaluate a fully integrated UAV-LiDAR method that utilizes context information
606 to improve the accuracy of AGB estimates of individual trees. The model performance consistently showed improve-
607 ments to AGB prediction when context-aware features were included as predictors. This phenomenon was observed
608 across regression models. The RMSE showed a reduction of 9.1 % in the SP-dataset and 4.0 % in the CP-dataset, while
609 the R^2 increased by 3.5 % in the SP-dataset and 3.2 % in the CP-dataset. The different degree of enhancement is con-
610 sidered to be related to the contrasting variability in context between the CP-dataset and the SP-dataset. Features
611 that provide information about the tree neighborhood (e.g. SL_i of tree height, average height of k-nearest trees) con-
612 tain useful information to improve predictions of different individual tree traits (e.g. DBH, AGB). This finding suggests
613 that the information retrieved from the local context serves as a proxy for underlying mechanisms that exert influence
614 on the variable of interest, i.e. tree heights adapt locally as a result of environmental and biotic processes [1, 39, 40].

615 Utilizing the spatial association of tree heights to define the local context range is a more effective approach
616 compared to methods that rely solely on plot-level data from artificially delineated units, such as the monitoring plot
617 size [20, 21, 24]. This is because contextual features may contribute to enhanced AGB predictions at larger scales
618 beyond the plot level. Moreover, as the method proposed uses metrics entirely native to the UAV-LiDAR dataset, it
619 does not rely on tailored process-specific indices (e.g. competition metrics) [23, 24, 25] or ancillary data sources (e.g.
620 biomes, conservation status, ecoregions) [12], making this approach more transferable to other regions or scales.

621 Regarding UAV-LiDAR data acquisition, we recommend establishing protocolized procedures for assessing PCD
622 quality, in line with recent suggestions [90]. Also, standardized methods for structural tree-trait data acquisition have
623 been proposed [120, 121]. However, as data collection surveys are commonly challenged by environmental conditions
624 and conducted by different field experts and protocols, the need to deal with noisy and disparate datasets is likely
625 to persist. Therefore, in order to successfully integrate ML models into real analysis pipelines in bio-geography, it
626 will be necessary to devise methods that are able to perform in the presence of label noise [122] and dataset shift
627 effects [94], as these, unlike benchmark datasets, are ubiquitous in real-world AGB applications.

628 A promising continuation within the scope of this research is to investigate the relative importance of different

629 context-based metrics in enhancing tree-level AGB predictions. This pathway may yield valuable insights into the
630 predictive power of various biotic and environmental factors as explanatory variables. Furthermore, since individual
631 adaptive responses can vary among tree populations [123], evaluating how diverging tree-height adaptations to the
632 local conditions can be linked to tree populations and genotypes with UAV-based methods seems a valuable endeavor
633 to pursue. In this line, recent work demonstrated that linking tree phenotyping to inheritable traits using UAV-based
634 methods is possible with high accuracy [124, 125, 126].

635 Finally, we recommend adopting a context-aware approach in the growing number of forest AGB mapping projects
636 [15, 127, 128]. Likewise, we recommend using metrics entirely locally computed (e.g. SL_i) to detect local patterns
637 and leverage their use, as suggested by Westerholt et al. (2018) [75]. In this way, the metric is sensitive to neighboring
638 differences while remaining totally independent from spatial structures beyond the border of the neighborhood (i.e.
639 the dataset as a whole).

640 Author contributions

641 Original conceptual framework: JCR and SO; experimental design: JCR; UAV-LiDAR data collection: JCR; field-based
642 data provision and curation: FS and MG; laser data processing: JCR; feature engineering, training and evaluation of
643 the machine learning models: JCR and SO; visualisation: JCR; supervision: AD; project administration: AD, NB and
644 JCR; writing—original draft preparation: JCR; writing—review and editing: SO, MG, FS, FG, KT, NB, AD, and JCR.

645 All authors have read and agreed to the published version of the manuscript.

646 Acknowledgements

647 Helpful discussions with Thomas Friberg, Daniel Kükenbrink and Moritz Bruggisser are gratefully acknowledged. Like-
648 wise, we acknowledge the contribution of the field workers, who are responsible for collecting the forest inventory
649 data on a regular basis, used here as ground-truth. This project received funding support from the Talent Program
650 Horizon 2020/Marie Skłodowska-Curie Actions and the DeepCrop project (UCPH Strategic plan 2023 Data + Pool).
651 MG also acknowledges funding by Swiss National Science Foundation project ICOS-CH Phase 3 (20F120_1982287).

652 Supporting Information

653 | Annex I: Location and Morphometry of Tree Assemblages

654 The spatial distribution of SL_i presents directional anisotropy, occupying preferential areas which seem to match
655 sheltered sectors of the forest, such as concave thalwegs. Figure 9 highlights two neighboring areas with contrasting
656 values of SL_i , indicating that surface hydrology processes and terrain exposure (i.e. terrain convexity) condition tree
657 growth at the group level.

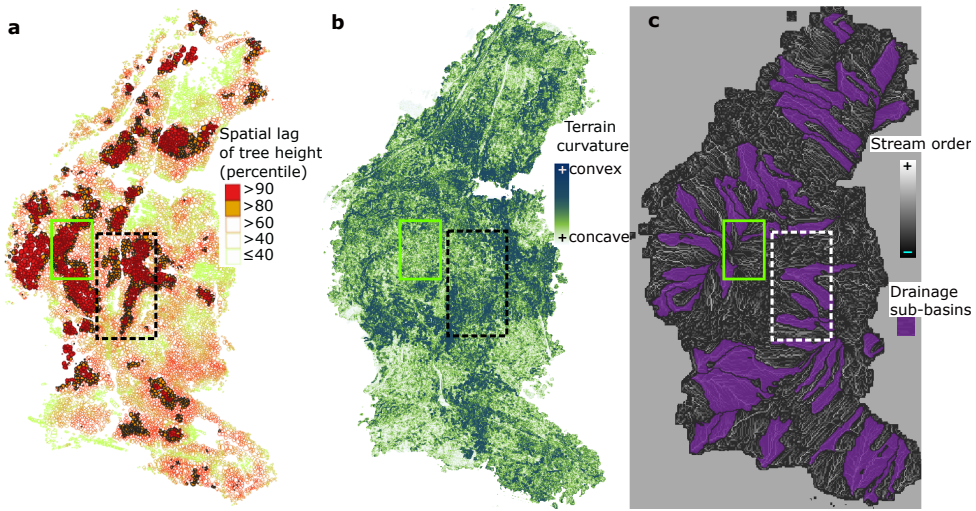


FIGURE 9 a: Spatial lag of tree height derived from the individual tree crown (ITC) polygon dataset. b: map of terrain curvature derived from point cloud data (PCD) ground-returns. c: Hydrological network (Strahler's stream order [129, 130]). In all three panels, the dashed box indicates an area favored by surface hydrological conditions, hosting an assemblage of trees in the >90 % percentile of spatial lag of tree height. The solid green box indicates an area at a hilltop, unfavored by surface hydrological processes, more exposed to windstorm disturbance, and hosting an assemblage of trees in the < 60% percentile of spatial lag of tree height.

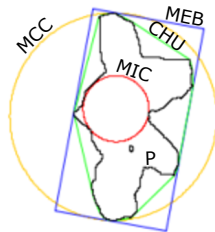


FIGURE 10 Calculation of elementary geometries fitted to an exemplary tree assemblage. P: polygon of tree assemblage (black line). MCC: minimum circumscribed circle (in green). MIC: maximum inscribed circle (in red). CHU: convex hull (in yellow). MEB: minimum enclosing box containing P (in blue).

658 The morphometric analysis was conducted by taking into account the outer borders of tree assemblages defined
 659 either by SL_i , or by local Moran's I_i (delineated as explained in Section 2.6; results shown in Figure 5). The 20 basic
 660 morphometric variables (Table 3) result from fitting elementary geometries to the tree assemblage polygon. The 20
 661 derived variables (Table 4) are adimensional parameters (except for concavity, in m^2) obtained by combining the basic
 662 parameters.

TABLE 3 Twenty basic morphometric variables derived from the tree assemblage polygon dataset (as described in [82]). P: tree assemblage polygon.

Basic parameters	Description	units
XPOL	Easting of P centroid	m
YPOL	Northing of P centroid	m
APOL	Area of P	m^2
PPOL	Perimeter of P	m
LPOL	Major axis' length of P	m
WPOL	Minor axis' length of P	m
N-S	North-South alignment of P, defined as $ \sin(\text{azimuth}) $ of major axis	\emptyset
ABOB	Area of the bounding box fully containing P	m^2
PBOB	Perimeter of the bounding box fully containing P	m
AMEB	Area of minimum enclosing box	m^2
PMEB	Perimeter of minimum enclosing box	m
ACHU	Area of the convex hull fully containing P	m^2
PCHU	Perimeter of the convex hull fully containing P	m
AMCC	Area of the minimum circumscribed circle enclosing P	m^2
PMCC	Perimeter of the minimum circumscribed circle enclosing P	m
RMCC	Radius of the minimum circumscribed circle enclosing P	m
AMIC	Area of the maximum inscribed circle enclosing P	m^2
PMIC	Perimeter of the maximum inscribed circle enclosing P	m
RMIC	Radius of the maximum inscribed circle enclosing P	m

TABLE 4 20 morphometric variables derived from the tree assemblage polygon dataset (as described in [82]). P: tree assemblage polygon. A: area of P. L: length of major axis of P. W: width of minor axis of P (i.e. width). ACHU: area of convex hull fully containing P. RMCC: radius of minimum circumscribed circle. PCHU: perimeter of convex hull fully containing P. AMEB: area of minimum enclosing box.

Derived parameters	Name	Definition	Source
LTWR	Length-to-width ratio	L/W	[98]
WTLR	Width-to-Length ratio	W/L	[99]
ELLF	Ellipticity Factor	$ L - W /(L + W)$	[100]
CIRR	Circularity Ratio	P^2/A	[101]
ZFOR	Zăvoianu's Form Factor	$(16A)/P^2$	[102]
COMF	Compactness Factor	$P/(4\pi A)^{0.5}$	[82]
MCIR	Miller's Circularity Ratio	$(4\pi A)/P^2$	[103]
DISM	Dispersion Measure	$1 - [(4\pi A)^{0.5}/P]$	[101]
COMI	Complexity Index	$1 - [(4\pi A)/P^2]$	[82]
HFOR	Horton's Form Factor	A/L^2	[98]
ELOF	Elongation Factor	$(4A/\pi)^{0.5}/L$	[104]
LEMR	Lemniscate Ratio	$(\pi L^2)/4A$	[105]
REGF	Regularity Factor	$(\pi LW)/4A$	[100]
SHAF	Shape Factor	$[(4\pi A)/P^2] \times (L/W)$	[100]
CONV	Convexity	$PCHU/P$	[106]
CONC	Concavity	$ACHU - A$	[81]
SOLI	Solidity	$A/ACHU$	[107]
RECT	Rectangularity	$A/AMEB$	[108]
ROUN	Roundness	$(4\pi A)/(PCHU)^2$	[106]
SPHE	Sphericity	$(4A/\pi)^{0.5}/(2 \times RMCC)$	[109]

664 | Annex II: Context Detection

665 The distance range selected around each tree to compute neighborhood metrics (i.e. context detection), was con-
 666 ducted based on the peak of significance (determined using the standard z-score) of local spatial autocorrelation
 667 (using Local Moran's I_i) as function of increasing distance, in steps of 10 m (as explained in Section 3.1).

668 Local Moran's I_i is a spatial statistic that relates attribute similarity to locational similarity, mapping the autocorre-
 669 lation of individual tree heights across the geographical space, as defined above (Eq. 1, Section 2.5.1). The expression
 670 below (Eq. 6) defines the z-score, which is used to measure the significance of tree-height clustering. Z-scores shows
 671 the significance of the clustering by subtracting the observed I_i values from the expectation (i.e. $E[I_i]$), and normal-
 672 izing over the standard deviation of I_i . This produces a distance metric in units of standard deviations. $E[I_i]$ is the
 673 expected value of local Moran's I_i under the null hypothesis of no spatial autocorrelation.

$$z_{score} = \frac{I_i - E[I_i]}{\sqrt{V[I_i]}}, \quad (6)$$

674 Neighborhood size was determined according to the significance of spatial autocorrelation (defined as local Moran's
675 I_i) as function of distance, via the standard z-score. Z-score measures the distance of a measured value from the ex-
676 pectation in units of standard deviation, under the assumption of randomly distributed values.

677 and the expected value of Moran's I under the null hypothesis of no spatial autocorrelation is:

$$E[I_i] = -\frac{\sum_{j=1}^m w_{i,j}}{m-1} = -\frac{1}{m-1}, \quad (7)$$

678 where m equals the total number of trees in the neighborhood. At large sample sizes (i.e. for increasing values of
679 m), the expected value approaches zero. The spatial weights allocated to each neighboring tree j are standardized [77],
680 such that for each tree i , $\sum_j w_{i,j} = 1$. The variance of local Moran's I_i is defined as the expectation of the square of I_i ,
681 minus the square of the expectations of I_i :

$$V[I_i] = E[I^2] - E[I_i]^2, \quad (8)$$

682 | Annex III: Training, Validation and Test

683 Nested cross-validation (NCV) [95] is an evaluation method for determining the accuracy of point estimates and
684 confidence intervals for prediction errors. How NCV is implemented is shown in Figure 11. The entire algorithmic
685 routine of NCV is presented immediately below, using pseudocode. The input data (i.e. X, Y) corresponds to the set of
686 predictors (i.e. X), and the target variable DBH (i.e. Y), respectively.

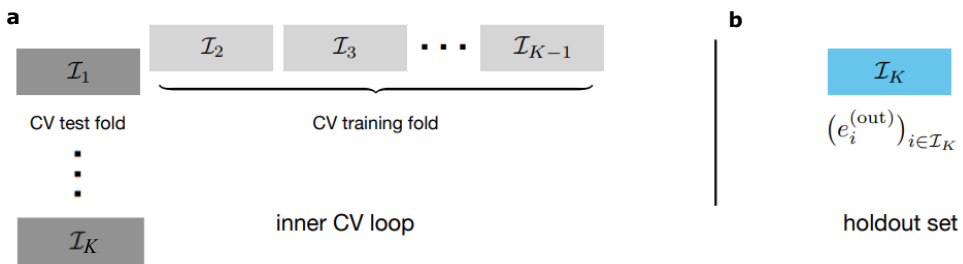


FIGURE 11 Visualization of 10-fold nested cross-validation (CV). **a:** at each of the K steps ($K = 10$), we perform standard cross-validation for model training (light grey folds), holding one of the folds out of the inner CV loop (dark grey fold). **b:** the fresh holdout folds (in blue) are never used for hyperparameter optimization or feature selection (figure adapted from Bates et al., 2021 [95]).

Algorithm 1: Nested cross-validation

Input: data (X, Y) , fitting algorithm A , loss function l , number of folds K , number of repetitions R

procedure Nested cross-validation (X, Y) // ▷ primary algorithm;

$es \leftarrow []$ // ▷ initialize empty vectors;

$a_list \leftarrow []$ // ▷ (a) terms;

$b_list \leftarrow []$ // ▷ (b) terms;

for $r \in \{1, \dots, R\}$ **do**

 Randomly assign points to folds I_1, \dots, I_K ;

for $k \in \{1, \dots, K\}$ **do**

 // ▷ outer CV loop;

$e^{(in)} \leftarrow$ inner cross-validation $(X, Y, \{I_1, \dots, I_K\} \setminus I_k)$ // ▷ inner CV loop;

$\hat{\theta} \leftarrow A((X_i, Y_i)_{i \in I \setminus I_k})$;

$e^{(out)} \leftarrow (l(\hat{f}(X_i, \hat{\theta}), Y_i))_{i \in I_k}$;

$b_list \leftarrow$ append($a_list, (mean(e^{(in)}) - mean(e^{(out)}))^2$);

$b_list \leftarrow$ append($b_list, var(e^{(out)})/|I_k|$);

$es \leftarrow$ append($es, e^{(in)}$)

$\widehat{MSE} \leftarrow mean(a_list) - mean(b_list)$;

$\widehat{Err}^{(NCV)} \leftarrow mean(es)$;

return: ($\widehat{Err}^{(NCV)}, \widehat{MSE}$) // ▷ prediction error estimate and MSE estimate;

procedure Inner cross-validation $(X, Y, \{I_1, \dots, I_{K-1}\})$ // ▷ inner cross-validation subroutine;

$e^{(in)} \leftarrow []$;

for $k \in \{1, \dots, K-1\}$ **do**

$\hat{\theta} \leftarrow A((X_i, Y_i)_{i \in I_1 \cup \dots \cup I_{K-1} \setminus k})$;

$e^{(temp)} \leftarrow (l(\hat{f}(X_i, \hat{\theta}), Y_i))_{i \in I_k}$;

$e^{(in)} \leftarrow$ append($e^{(in)}, e^{(temp)}$)

return: $e^{(in)}$;

Output: Nested cross-validation (X, Y)

Annex IV: Distribution Shift Between CP-trees and SP-trees

By morphological tree traits, we refer to the structural tree parameters considered in the study (i.e. tree height and DBH). Here below, we visualize the joint distributions of DBH and tree height in the two datasets considered in order to highlight how differently distributed they are.

The joint distributions of morphological tree traits DBH and tree height in both CP and SP datasets show a shift between the two [94]. For instance, the kernel probability distribution of heights shows that the SP-dataset contains a higher amount of short trees (i.e. heights $\in (3, \dots, 8)$ m), that cover a wide range of DBH values. Also, the range of DBH is broader in the SP-dataset compared to the CP-dataset, and the instances do not exhibit an accumulation in the center as evident as the one observed in the CP-dataset.

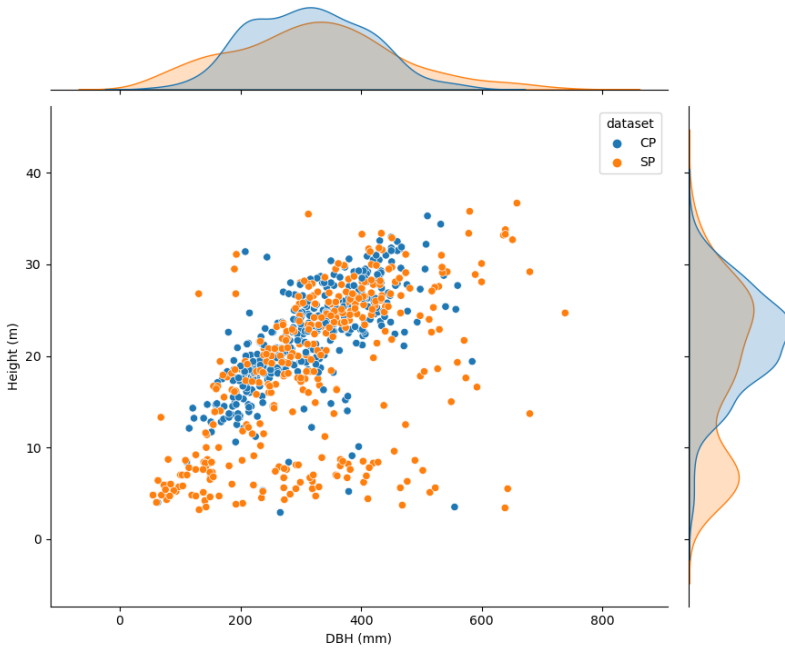


FIGURE 12 Joint distributions of diameter at breast-height (DBH) and tree height from field-based inventory data. It should be noted that the two datasets are differently distributed—i.e. there is a dataset shift [94] between sampling plots (SP) and control plots (CP) datasets.

697 | **Annex V: Elevation map of the study site**

698 We provide the digital elevation model of the study area (Figure 13, a) to understand differences in flight heights
 699 (Figure 2) and to complement the information given on terrain exposure and surface hydrology (Figure 9). Figure 13,
 700 (b) shows the five rejected SP-plots and one valid (i.e. SP-18), for comparison. Among the rejected SP-plots, 1, 2, 9 and
 701 10 show an insufficiently descriptive CHM, while SP-14 shows an intractable allocation of ground-based labels. All
 702 five rejected SP-plots were discarded before starting the modelling process, so they did not take part in the regression
 703 experiments.

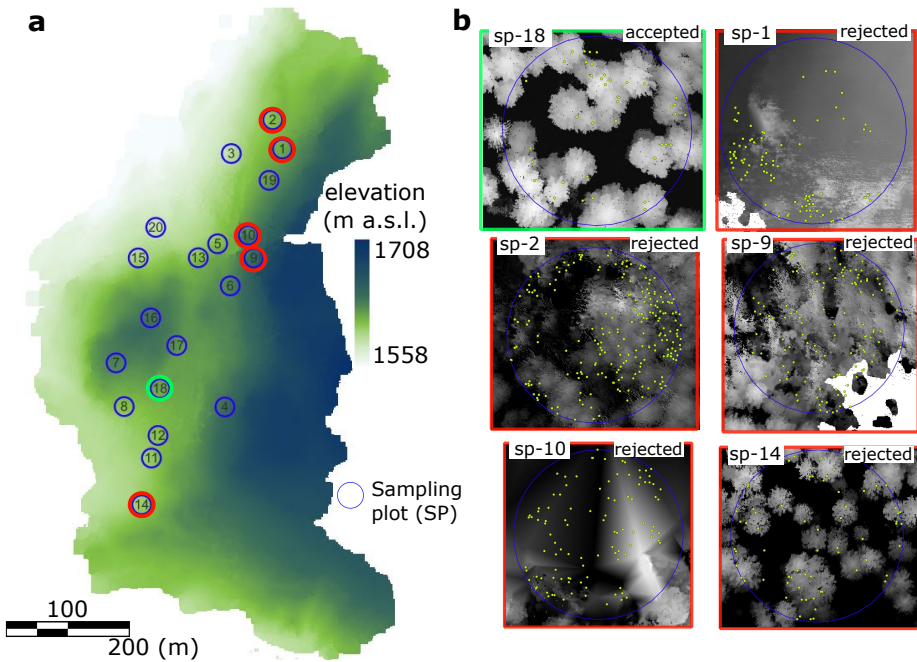


FIGURE 13 a: Digital elevation model of the stud area. a.s.l.: elevation above sea level, in m. The blue circles represent the SP-plots, numbered b their ID code. The green and red circles refer to the plots shown in panel b. b: five SP-plots rejected and one valid (SP-18) given for comparison of contrasting quality of canopy height models, derived from the UAV-LiDAR point cloud data. In all six SP-plots, the yellow dots indicate the location of tree stems according to the field-based inventory.

704 **references**

- 705 [1] Fatichi S, Pappas C, Zscheischler J, Leuzinger S. Modelling carbon sources and sinks in terrestrial vegetation. *New*
706 *Phytologist* 2019;221(2):652–668.
- 707 [2] Pörtner HO, Roberts DC, Adams H, Adler C, Aldunce P, Ali E, et al. *Climate change 2022: Impacts, adaptation and*
708 *vulnerability*. IPCC Geneva, Switzerland.; 2022.
- 709 [3] Gundersen P, Thybring EE, Nord-Larsen T, Vesterdal L, Nadelhoffer KJ, Johannsen VK. Old-growth forest carbon sinks
710 overestimated. *Nature* 2021;591(7851):E21–E23.
- 711 [4] Friedlingstein P, Jones MW, O'sullivan M, Andrew RM, Hauck J, Peters GP, et al. Global carbon budget 2019. *Earth*
712 *System Science Data* 2019;11(4):1783–1838.
- 713 [5] Baccini A, Walker W, Carvalho L, Farina M, Sulla-Menashe D, Houghton R. Tropical forests are a net carbon source
714 based on aboveground measurements of gain and loss. *Science* 2017;358(6360):230–234.
- 715 [6] Duncanson L, Armston J, Disney M, Avitabile V, Barbier N, Calders K, et al. The importance of consistent global forest
716 aboveground biomass product validation. *Surveys in geophysics* 2019;40:979–999.
- 717 [7] Brandt M, Tucker CJ, Kariryaa A, Rasmussen K, Abel C, Small J, et al. An unexpectedly large count of trees in the West
718 African Sahara and Sahel. *Nature* 2020;587(7832):78–82.
- 719 [8] Oehmcke S, Li L, Revenga JC, Nord-Larsen T, Trepekli K, Gieseke F, et al. Deep learning based 3D point cloud regres-
720 sion for estimating forest biomass. In: *Proceedings of the 30th International Conference on Advances in Geographic*
721 *Information Systems*; 2022. p. 1–4.
- 722 [9] Reiner F, Brandt M, Tong X, Skole D, Kariryaa A, Ciais P, et al. More than one quarter of Africa's tree cover is found
723 outside areas previously classified as forest. *Nature Communications* 2023;14(1):2258.
- 724 [10] H Nguyen T, Jones S, Soto-Berelov M, Haywood A, Hislop S. Landsat time-series for estimating forest aboveground
725 biomass and its dynamics across space and time: A review. *Remote Sensing* 2019;12(1):98.
- 726 [11] Réjou-Méchain M, Barbier N, Couteron P, Ploton P, Vincent G, Herold M, et al. Upscaling forest biomass from field to
727 satellite measurements: sources of errors and ways to reduce them. *Surveys in Geophysics* 2019;40(4):881–911.
- 728 [12] Wang CJ, Zhang ZX, Wan JZ. Vulnerability of global forest ecoregions to future climate change. *Global Ecology and*
729 *Conservation* 2019;20:e00760.
- 730 [13] Melo J, Baker T, Nemitz D, Quegan S, Ziv G. Satellite-based global maps are rarely used in forest reference levels
731 submitted to the UNFCCC. *Environmental Research Letters* 2023;18(3):034021.
- 732 [14] Bruggisser M, Hollaus M, Kükenbrink D, Pfeifer N. Comparison of forest structure metrics derived from UAV lidar and
733 ALS data. *ISPRS Annals of the Photogrammetry, Remote Sensing and Spatial Information Sciences* 2019;4:325–332.
- 734 [15] Labrière N, Davies SJ, Disney MI, Duncanson LI, Herold M, Lewis SL, et al. Toward a forest biomass reference measure-
735 ment system for remote sensing applications. *Global Change Biology* 2023;29(3):827–840.
- 736 [16] Hyyppä E, Yu X, Kaartinen H, Hakala T, Kukko A, Vastaranta M, et al. Comparison of backpack, handheld, under-canopy
737 UAV, and above-canopy UAV laser scanning for field reference data collection in boreal forests. *Remote Sensing*
738 2020;12(20):3327.
- 739 [17] Li N, Ho CP, Xue J, Lim LW, Chen G, Fu YH, et al. A Progress Review on Solid-State LiDAR and Nanophotonics-Based
740 LiDAR Sensors. *Laser & Photonics Reviews* 2022;16(11):2100511.
- 741 [18] Santini F, Kefauver SC, Resco de Dios V, Araus JL, Voltas J. Using unmanned aerial vehicle-based multispectral, RGB
742 and thermal imagery for phenotyping of forest genetic trials: A case study in *Pinus halepensis*. *Annals of Applied*
743 *Biology* 2019;174(2):262–276.

- 744 [19] Yao W, Krull J, Krzystek P, Heurich M. Sensitivity analysis of 3D individual tree detection from LiDAR point clouds of
745 temperate forests. *Forests* 2014;5(6):1122–1142.
- 746 [20] Hao Y, Widagdo FRA, Liu X, Quan Y, Dong L, Li F. Individual tree diameter estimation in small-scale forest inventory
747 using UAV laser scanning. *Remote Sensing* 2020;13(1):24.
- 748 [21] Yang Z, Liu Q, Luo P, Ye Q, Sharma RP, Duan G, et al. Nonlinear mixed-effects height to crown base model based on both
749 airborne LiDAR and field datasets for *Picea crassifolia* Kom trees in northwest China. *Forest Ecology and Management*
750 2020;474:118323.
- 751 [22] Liu X, Hao Y, Widagdo FRA, Xie L, Dong L, Li F. Predicting height to crown base of *Larix olgensis* in Northeast China
752 Using UAV-LiDAR data and nonlinear mixed effects models. *Remote Sensing* 2021;13(9):1834.
- 753 [23] Sun S, Cao QV, Cao T. Evaluation of distance-independent competition indices in predicting tree survival and diameter
754 growth. *Canadian Journal of Forest Research* 2019;49(5):440–446.
- 755 [24] Zhang B, Sajjad S, Chen K, Zhou L, Zhang Y, Yong KK, et al. Predicting tree height-diameter relationship from relative
756 competition levels using quantile regression models for Chinese fir (*Cunninghamia lanceolata*) in Fujian province, China.
757 *Forests* 2020;11(2):183.
- 758 [25] Lo CS, Lin C. Growth-competition-based stem diameter and volume modeling for tree-level forest inventory using
759 airborne LiDAR data. *IEEE Transactions on Geoscience and Remote Sensing* 2012;51(4):2216–2226.
- 760 [26] Andersen HE, McGaughey RJ, Reutebuch SE. Estimating forest canopy fuel parameters using LIDAR data. *Remote
761 sensing of Environment* 2005;94(4):441–449.
- 762 [27] Næsset E, Økland T. Estimating tree height and tree crown properties using airborne scanning laser in a boreal nature
763 reserve. *Remote Sensing of Environment* 2002;79(1):105–115.
- 764 [28] Rijal B, Weiskittel AR, Kershaw Jr JA. Development of height to crown base models for thirteen tree species of the
765 North American Acadian Region. *The Forestry Chronicle* 2012;88(1):60–73.
- 766 [29] Xu D, Wang H, Xu W, Luan Z, Xu X. LiDAR applications to estimate forest biomass at individual tree scale: Opportunities,
767 challenges and future perspectives. *Forests* 2021;12(5):550.
- 768 [30] Biging GS, Dobbertin M. Evaluation of competition indices in individual tree growth models. *Forest science*
769 1995;41(2):360–377.
- 770 [31] Antonio N, Tome M, Tome J, Soares P, Fontes L. Effect of tree, stand, and site variables on the allometry of *Eucalyptus*
771 *globulus* tree biomass. *Canadian Journal of Forest Research* 2007;37(5):895–906.
- 772 [32] Silvertown J. Plant coexistence and the niche. *Trends in Ecology & evolution* 2004;19(11):605–611.
- 773 [33] Pachepsky E, Bown JL, Eberst A, Bausenwein U, Millard P, Squire GR, et al. Consequences of intraspecific variation
774 for the structure and function of ecological communities Part 2: Linking diversity and function. *Ecological Modelling*
775 2007;207(2-4):277–285.
- 776 [34] Duncanson L, Kellner JR, Armston J, Dubayah R, Minor DM, Hancock S, et al. Aboveground biomass density mod-
777 els for NASA's Global Ecosystem Dynamics Investigation (GEDI) lidar mission. *Remote Sensing of Environment*
778 2022;270:112845.
- 779 [35] Liu S, Brandt M, Nord-Larsen T, Chave J, Reiner F, Lang N, et al. The overlooked contribution of trees outside forests
780 to tree cover and woody biomass across Europe. Preprint 2023;.
- 781 [36] Anselin L. Local indicators of spatial association—LISA. *Geographical analysis* 1995;27(2):93–115.

- 782 [37] Valladares F, Arrieta S, Aranda I, Lorenzo D, Sánchez-Gómez D, Tena D, et al. Shade tolerance, photoinhibition sensitivity
783 and phenotypic plasticity of *Ilex aquifolium* in continental Mediterranean sites. *Tree physiology* 2005;25(8):1041–
784 1052.
- 785 [38] Valladares F, Dobarro I, Sánchez-Gomez D, Pearcy RW. Photoinhibition and drought in Mediterranean woody saplings:
786 scaling effects and interactions in sun and shade phenotypes. *Journal of Experimental Botany* 2005;56(411):483–494.
- 787 [39] Goebes P, Schmidt K, Seitz S, Both S, Bruelheide H, Erfmeier A, et al. The strength of soil-plant interactions under
788 forest is related to a Critical Soil Depth. *Scientific Reports* 2019;9(1):8635.
- 789 [40] Green JK, Keenan TF. The limits of forest carbon sequestration. *Science* 2022;376(6594):692–693.
- 790 [41] Anselin L, Rey SJ. Perspectives on spatial data analysis. In: *Perspectives on spatial data analysis* Springer; 2010,p.
791 1–20.
- 792 [42] Valladares F, Gianoli E, Gómez JM. Ecological limits to plant phenotypic plasticity. *New phytologist* 2007;176(4):749–
793 763.
- 794 [43] Schiefer F, Kattenborn T, Frick A, Frey J, Schall P, Koch B, et al. Mapping forest tree species in high resolution UAV-based
795 RGB-imagery by means of convolutional neural networks. *ISPRS Journal of Photogrammetry and Remote Sensing*
796 2020;170:205–215.
- 797 [44] Marques O, Barenholtz E, Charvillat V. Context modeling in computer vision: techniques, implications, and applications.
798 *Multimedia Tools and Applications* 2011;51:303–339.
- 799 [45] Zhao R, Ouyang W, Li H, Wang X. Saliency Detection by Multi-Context Deep Learning. In: *Proceedings of the IEEE*
800 *Conference on Computer Vision and Pattern Recognition (CVPR)*; 2015. p. 1265–1274.
- 801 [46] Luo W, Li Y, Urtasun R, Zemel R. Understanding the effective receptive field in deep convolutional neural networks.
802 *Advances in neural information processing systems* 2016;29.
- 803 [47] Yang W, Tan RT, Feng J, Liu J, Guo Z, Yan S. Deep joint rain detection and removal from a single image. In: *Proceedings*
804 *of the IEEE conference on computer vision and pattern recognition*; 2017. p. 1357–1366.
- 805 [48] Liu YF, Jaw DW, Huang SC, Hwang JN. DesnowNet: Context-aware deep network for snow removal. *IEEE Transactions*
806 *on Image Processing* 2018;27(6):3064–3073.
- 807 [49] Chu HJ, Wu CF, Lin YP. Incorporating spatial autocorrelation with neural networks in empirical land-use change models.
808 *Environment and Planning B: Planning and Design* 2013;40(3):384–404.
- 809 [50] Reichstein M, Camps-Valls G, Stevens B, Jung M, Denzler J, Carvalhais N. Deep learning and process understanding
810 for data-driven Earth system science. *Nature* 2019;566(7743):195–204.
- 811 [51] Chakraborti S, Das DN, Mondal B, Shafizadeh-Moghadam H, Feng Y. A neural network and landscape metrics to
812 propose a flexible urban growth boundary: A case study. *Ecological indicators* 2018;93:952–965.
- 813 [52] Heiskanen J, C B, N B, C C, H C, B G, et al. The Integrated Carbon Observation System in Europe. *Bulletin of the*
814 *American Meteorological Society* 2022;103(3):E855–E872.
- 815 [53] Juszczak T, Voluntary National report to UNF1 from Switzerland; 2019. [https://www.un.org/esa/forests/documents/
816 national-reports](https://www.un.org/esa/forests/documents/national-reports).
- 817 [54] Burri S. Long-Term Environmental Research–The Davos-Seehornwald Site. *ETH Zurich Research collection* 2019;.
- 818 [55] WSL, Long-term Forest Ecosystem Research (WSL); 2023. [https://www.wsl.ch/en/about-wsl/organisation/
819 programmes-and-initiatives/](https://www.wsl.ch/en/about-wsl/organisation/programmes-and-initiatives/).

- 820 [56] TreeNet, Biological drought and growth indicator network; 2023. <https://treenet.info/>.
- 821 [57] ETH-Zurich, Biological drought and growth indicator network; 2023. <https://www.swissfluxnet.ethz.ch/>.
- 822 [58] ICOS, Integrated Carbon Observation System; 2023. <https://www.icos-cp.eu/>.
- 823 [59] ICP-Forest, International Co-operative Programme on Assessment and Monitoring of Air Pollution Effects on Forests;
824 2023. <http://icp-forests.net/>.
- 825 [60] eLTER, Integrated European Long-Term Ecosystem, critical zone and socio-ecological Research; 2023. <https://elter-ri.eu/>.
- 826
- 827 [61] Revengea JC, Trepekli K, Oehmcke S, Jensen R, Li L, Igel C, et al. Above-Ground Biomass Prediction for Croplands at a
828 Sub-Meter Resolution Using UAV-LiDAR and Machine Learning Methods. *Remote Sensing* 2022;14(16):3912.
- 829 [62] Davidson L, Mills J, Haynes I, Augarde C, Bryan P, Douglas M. Airborne to UAS LiDAR: An analysis of UAS LiDAR
830 ground control targets. *ISPRS Geospatial Week 2019*;
- 831 [63] Swiss Federal Institute for Forest S, (WSL) LR, Methods of the Sanasilva Inventory; 2023. <https://www.wsl.ch/en/forest/forest-development-and-monitoring/sanasilva-forest-health-inventory/methods-of-the-sanasilva-inventory.html>.
- 832
- 833
- 834 [64] Hunziker S, Begert M, Scherrer SC, Rigling A, Gessler A. Below average midsummer to early autumn precipitation
835 evolved into the main driver of sudden Scots pine vitality decline in the Swiss Rhône valley. *Frontiers in Forests and*
836 *Global Change* 2022;p. 103.
- 837 [65] ICOS-ETC, Instruction on ancillary vegetation measurements in forest; 2023. <http://www.icos-etc.eu/icos/documents/instructions/ancfor>.
- 838
- 839 [66] Chen Q GP Baldocchi D, M K. Isolating Individual Trees in a Savanna Woodland Using Small Footprint Lidar Data. In:
840 *Photogrammetric Engineering and Remote Sensing*, 72(8): 923-932; 2006. p. 923-932.
- 841 [67] GreenValley-International. LiDAR360 User Guide. California, USA; January 2021, www.greenvalletintl.com.
- 842 [68] Breunig MM, Kriegel HP, Ng RT, Sander J. LOF: identifying density-based local outliers. In: *Proceedings of the 2000*
843 *ACM SIGMOD international conference on Management of data*; 2000. p. 93-104.
- 844 [69] Liu FT, Ting KM, Zhou ZH. Isolation forest. In: *2008 eighth iee international conference on data mining IEEE*; 2008.
845 p. 413-422.
- 846 [70] Anselin L, Syabri I, Kho Y. GeoDa: an introduction to spatial data analysis. In: *Handbook of applied spatial analysis: Software tools, methods and applications* Springer; 2009.p. 73-89.
- 847
- 848 [71] Da Silva BC, Basso EW, Bazzan AL, Engel PM. Dealing with non-stationary environments using context detection. In:
849 *Proceedings of the 23rd international conference on Machine learning*; 2006. p. 217-224.
- 850 [72] Fu WJ, Jiang PK, Zhou GM, Zhao KL. Using Moran's I and GIS to study the spatial pattern of forest litter carbon density
851 in a subtropical region of southeastern China. *Biogeosciences* 2014;11(8):2401-2409.
- 852 [73] Cressie N. *Statistics for spatial data*. John Wiley & Sons; 2015.
- 853 [74] Getis A, Ord JK. The analysis of spatial association by use of distance statistics. In: *Perspectives on spatial data analysis*
854 Springer; 2010.p. 127-145.
- 855 [75] Westerholt R, Resch B, Mocnik FB, Hoffmeister D. A statistical test on the local effects of spatially structured variance.
856 *International Journal of Geographical Information Science* 2018;32(3):571-600.

- 857 [76] Hastie TJ. Generalized additive models. In: *Statistical models in S* Routledge; 2017.p. 249–307.
- 858 [77] Anselin L, et al. *Spatial econometrics. A companion to theoretical econometrics* 2001;310330.
- 859 [78] Beven KJ, Kirkby MJ. A physically based, variable contributing area model of basin hydrology/Un modèle à base
860 physique de zone d'appel variable de l'hydrologie du bassin versant. *Hydrological sciences journal* 1979;24(1):43–69.
- 861 [79] Kopecký M, Macek M, Wild J. Topographic Wetness Index calculation guidelines based on measured soil moisture and
862 plant species composition. *Science of the Total Environment* 2021;757:143785.
- 863 [80] ESRI. *ArcGis Pro: Implementation Guide*. Redlands, California; 2021, www.esri.com.
- 864 [81] Landini G, *Particles8 class: An ImageJ plugin for estimating various statistics of binary 8- connected particles.*; 2010.
865 <https://blog.bham.ac.uk/intellimic/g-landini-software>, accessed on November 25, 2022.
- 866 [82] Güler C, Beyhan B, Tağa H. PolyMorph-2D: An open-source GIS plug-in for morphometric analysis of vector-based
867 2D polygon features. *Geomorphology* 2021;386:107755.
- 868 [83] Steiniger S, Blake L, *OpenJUMP software.*; www.openjump.org.
- 869 [84] Freund Y, Schapire RE. A decision-theoretic generalization of on-line learning and an application to boosting. *Journal*
870 *of computer and system sciences* 1997;55(1):119–139.
- 871 [85] Friedman JH. Greedy function approximation: a gradient boosting machine. *Annals of statistics* 2001;p. 1189–1232.
- 872 [86] Tibshirani R. Regression shrinkage and selection via the lasso. *Journal of the Royal Statistical Society: Series B (Method-*
873 *ological)* 1996;58(1):267–288.
- 874 [87] Ho TK. Random decision forests. In: *Proceedings of 3rd international conference on document analysis and recognition*,
875 *vol. 1 IEEE*; 1995. p. 278–282.
- 876 [88] Schapire RE. Explaining adaboost. *Empirical Inference: Festschrift in Honor of Vladimir N Vapnik* 2013;p. 37–52.
- 877 [89] Vidaurre D, Bielza C, Larranaga P. A survey of L1 regression. *International Statistical Review* 2013;81(3):361–387.
- 878 [90] Demol M, Verbeeck H, Gielen B, Armston J, Burt A, Disney M, et al. Estimating forest above-ground biomass with
879 terrestrial laser scanning: Current status and future directions. *Methods in Ecology and Evolution* 2022;13(8):1628–
880 1639.
- 881 [91] Dalponte M, Coomes DA. Tree-centric mapping of forest carbon density from airborne laser scanning and hyperspectral
882 data. *Methods in ecology and evolution* 2016;7(10):1236–1245.
- 883 [92] Gryc V, Horáček P. Variability in density of spruce (*Picea abies* [L.] Karst.) wood with the presence of reaction wood.
884 *Journal of forest science* 2007;53(3):129–137.
- 885 [93] Scrinzi G, Galvagni D, Marzullo L. I nuovi modelli dendrometrici per la stima delle masse assestamentali in Provincia di
886 Trento. *Provincia autonoma di Trento. Servizio foreste e fauna*; 2010.
- 887 [94] Quionero-Candela J, Sugiyama M, Schwaighofer A, Lawrence ND. *Data Set Shift in Machine Learning*. MIT Press, Cam-
888 bridge, Massachusetts; 2009. [http://www.acad.bg/ebook/ml/The.MIT.Press.Dataset.Shift.in.Machine.Learning.](http://www.acad.bg/ebook/ml/The.MIT.Press.Dataset.Shift.in.Machine.Learning.Feb.2009.eBook-DDU.pdf)
889 [Feb.2009.eBook-DDU.pdf](http://www.acad.bg/ebook/ml/The.MIT.Press.Dataset.Shift.in.Machine.Learning.Feb.2009.eBook-DDU.pdf).
- 890 [95] Bates S, Hastie T, Tibshirani R. Cross-validation: what does it estimate and how well does it do it? *arXiv preprint*
891 *arXiv:210400673* 2021;.
- 892 [96] Wilcoxon F. *Individual comparisons by ranking methods*. Springer; 1992.

- 893 [97] Cliff N. Dominance statistics: Ordinal analyses to answer ordinal questions. *Psychological bulletin* 1993;114(3):494.
- 894 [98] Horton RE. Drainage-basin characteristics. *Transactions, American geophysical union* 1932;13(1):350–361.
- 895 [99] Zingg T. Beitrag zur schotteranalyse. PhD thesis, ETH Zurich; 1935.
- 896 [100] Buendia P, Soler C, Paolicchi F, Gago G, Urquieta B, Pérez-Sánchez F, et al. Morphometric characterization and
897 classification of alpaca sperm heads using the Sperm-Class Analyzer® computer-assisted system. *Theriogenology*
898 2002;57(4):1207–1218.
- 899 [101] Attneave F, Arnoult MD. The quantitative study of shape and pattern perception. *Psychological bulletin*
900 1956;53(6):452.
- 901 [102] Zăvoianu I. Morfometria bazinelor hidrografice. Editura Academiei Republicii Socialiste România; 1978.
- 902 [103] Miller VC. A QUANTITATIVE GEOMORPHIC STUDY OF DRAINAGE BASIN CHARACTERISTICS IN THE CLINCH
903 MOUNTAIN AREA VIRGINIA AND TENNESSEE. Columbia Univ New York; 1953.
- 904 [104] Schumm SA. Evolution of drainage systems and slopes in badlands at Perth Amboy, New Jersey. *Geological society of*
905 *America bulletin* 1956;67(5):597–646.
- 906 [105] Chorley RJ, Malm E Donald E, Pogorzelski HA. A new standard for estimating drainage basin shape. *American Journal*
907 *of Science* 1957;255:138–141.
- 908 [106] Horgan GW, Glasbey CA. Uses of digital image analysis in electrophoresis. *Electrophoresis* 1995;16(1):298–305.
- 909 [107] Zunic J, Rosin PL. A new convexity measure for polygons. *IEEE Transactions on Pattern Analysis and Machine Intelli-*
910 *gence* 2004;26(7):923–934.
- 911 [108] Rosin PL. Measuring rectangularity. *Machine Vision and Applications* 1999;11:191–196.
- 912 [109] Wadell H. Volume, shape, and roundness of quartz particles. *The Journal of Geology* 1935;43(3):250–280.
- 913 [110] Altmann A, Toloşi L, Sander O, Lengauer T. Permutation importance: a corrected feature importance measure. *Bioin-*
914 *formatics* 2010;26(10):1340–1347.
- 915 [111] Pillar VD, Duarte LdS, Sosinski EE, Joner F. Discriminating trait-convergence and trait-divergence assembly patterns
916 in ecological community gradients. *Journal of Vegetation Science* 2009;20(2):334–348.
- 917 [112] Guillén-Escribà C, Schneider FD, Schmid B, Tedder A, Morsdorf F, Furrer R, et al. Remotely sensed between-individual
918 functional trait variation in a temperate forest. *Ecology and Evolution* 2021;11(16):10834–10867.
- 919 [113] Zheng Z, Zeng Y, Schuman MC, Jiang H, Schmid B, Schaepman ME, et al. Individual tree-based vs pixel-based ap-
920 proaches to mapping forest functional traits and diversity by remote sensing. *International Journal of Applied Earth*
921 *Observation and Geoinformation* 2022;114:103074.
- 922 [114] Ma X, Migliavacca M, Wirth C, Bohn FJ, Huth A, Richter R, et al. Monitoring plant functional diversity using the
923 reflectance and echo from space. *Remote Sensing* 2020;12(8):1248.
- 924 [115] He X, Zemel RS, Carreira-Perpinán MA. Multiscale conditional random fields for image labeling. In: Proceedings of
925 the 2004 IEEE Computer Society Conference on Computer Vision and Pattern Recognition, 2004. CVPR 2004., vol. 2
926 IEEE; 2004. p. II-II.
- 927 [116] Yu F, Koltun V. Multi-scale context aggregation by dilated convolutions. arXiv preprint arXiv:151107122 2015;.
- 928 [117] Abelleira Martínez OJ, Fremier AK, Günter S, Ramos Bendaña Z, Vierling L, Galbraith SM, et al. Scaling up functional
929 traits for ecosystem services with remote sensing: concepts and methods. *Ecology and Evolution* 2016;6(13):4359–
930 4371.

- 931 [118] Kraft NJ, Adler PB, Godoy O, James EC, Fuller S, Levine JM. Community assembly, coexistence and the environmental
932 filtering metaphor. *Functional ecology* 2015;29(5):592–599.
- 933 [119] Berrar D. *Cross-Validation*; 2019.
- 934 [120] Valbuena R, O'Connor B, Zellweger F, Simonson W, Vihervaara P, Maltamo M, et al. Standardizing ecosystem morpho-
935 logical traits from 3D information sources. *Trends in Ecology & Evolution* 2020;35(8):656–667.
- 936 [121] Fahey RT, Atkins JW, Gough CM, Hardiman BS, Nave LE, Tallant JM, et al. Defining a spectrum of integrative trait-based
937 vegetation canopy structural types. *Ecology letters* 2019;22(12):2049–2059.
- 938 [122] Qu Y, Mo S, Niu J. Dat: Training deep networks robust to label-noise by matching the feature distributions. In: *Pro-
939 ceedings of the IEEE/CVF Conference on Computer Vision and Pattern Recognition*; 2021. p. 6821–6829.
- 940 [123] Cooper HF, Grady KC, Cowan JA, Best RJ, Allan GJ, Whitham TG. Genotypic variation in phenological plasticity: Re-
941 ciprocal common gardens reveal adaptive responses to warmer springs but not to fall frost. *Global change biology*
942 2019;25(1):187–200.
- 943 [124] Ludovisi R, Tauro F, Salvati R, Khoury S, Mugnozza Scarascia G, Harfouche A. UAV-based thermal imaging for high-
944 throughput field phenotyping of black poplar response to drought. *Frontiers in plant science* 2017;8:1681.
- 945 [125] Rallo P, de Castro AI, López-Granados F, Morales-Sillero A, Torres-Sánchez J, Jiménez MR, et al. Exploring UAV-imagery
946 to support genotype selection in olive breeding programs. *Scientia Horticulturae* 2020;273:109615.
- 947 [126] Sankey T, Hultine K, Blasini D, Koepke D, Bransky N, Grady K, et al. UAV thermal image detects genetic trait differences
948 among populations and genotypes of Fremont cottonwood (*Populus fremontii*, Salicaceae). *Remote Sensing in Ecology
949 and Conservation* 2021;7(2):245–258.
- 950 [127] Quegan S, Le Toan T, Chave J, Dall J, Exbrayat JF, Minh DHT, et al. The European Space Agency BIOMASS mission:
951 Measuring forest above-ground biomass from space. *Remote Sensing of Environment* 2019;227:44–60.
- 952 [128] Dubayah R, Luthcke S, Sabaka T, Nicholas J, Preaux S, Hofton M, GEDI L3 Gridded Land Surface Metrics. Version;
953 2021.
- 954 [129] Horton RE. Erosional development of streams and their drainage basins; hydrophysical approach to quantitative mor-
955 phology. *Geological society of America bulletin* 1945;56(3):275–370.
- 956 [130] Strahler AN. Hypsometric (area-altitude) analysis of erosional topography. *Geological society of America bulletin*
957 1952;63(11):1117–1142.